

Macromolecular tissue volume mapping of lateral geniculate nucleus subdivisions in living human brains

Hiroki Oishi^{a,b,c,*}, Hiromasa Takemura^{a,b,d,e,*}, Kaoru Amano^{a,b,f}

^a Center for Information and Neural Networks (CiNet), Advanced ICT Research Institute, National Institute of Information and Communications Technology, Suita 565-0871, Japan

^b Graduate School of Frontier Biosciences, Osaka University, Suita 565-0871, Japan

^c Department of Psychology, University of California, Berkeley, Berkeley, CA 94704, United States

^d Division of Sensory and Cognitive Brain Mapping, Department of System Neuroscience, National Institute for Physiological Sciences, Okazaki 444-8585, Japan

^e Department of Physiological Sciences, School of Life Science, SOKENDAI (The Graduate University for Advanced Studies), Hayama 240-0193, Japan

^f Graduate School of Information Science and Technology, The University of Tokyo, Tokyo 113-8656, Japan

ARTICLE INFO

Keywords:

Lateral geniculate nucleus
Magnocellular
Parvocellular
Structural MRI
Functional MRI
Visual system

ABSTRACT

The lateral geniculate nucleus (LGN) is a key thalamic nucleus in the visual system, which has an important function in relaying retinal visual input to the visual cortex. The human LGN is composed mainly of magnocellular (M) and parvocellular (P) subdivisions, each of which has different stimulus selectivity in neural response properties. Previous studies have discussed the potential relationship between LGN subdivisions and visual disorders based on psychophysical data on specific types of visual stimuli. However, these relationships remain speculative because non-invasive measurements of these subdivisions are difficult due to the small size of the LGN. Here we propose a method to identify these subdivisions by combining two structural MR measures: high-resolution proton-density weighted images and macromolecular tissue volume (MTV) maps. We defined the M and P subdivisions based on MTV fraction data and tested the validity of the definition by (1) comparing the data with that from human histological studies, (2) comparing the data with functional magnetic resonance imaging measurements on stimulus selectivity, and (3) analyzing the test-retest reliability. The findings demonstrated that the spatial organization of the M and P subdivisions was consistent across subjects and in line with LGN subdivisions observed in human histological data. Moreover, the difference in stimulus selectivity between the subdivisions identified using MTV was consistent with previous physiology literature. The definition of the subdivisions based on MTV was shown to be robust over measurements taken on different days. These results suggest that MTV mapping is a promising approach for evaluating the tissue properties of LGN subdivisions in living humans. This method potentially will enable neuroscientific and clinical hypotheses about the human LGN subdivisions to be tested.

1. Introduction

Over the past several decades, progress in functional and structural neuroimaging has enabled detailed mapping methods for various cortical visual areas in the living human brain (DeYoe et al., 1994; Engel et al., 1994; Sereno et al., 1995, 2013; Dumoulin and Wandell, 2008; Wandell and Winawer, 2011; Glasser et al., 2016; Benson and Winawer, 2018). These methods have provided important insights on how properties of the cortical visual areas are related to visual perception and dysfunctions (Wandell and Winawer, 2015). However, to date, few neuroimaging methods have been established to investigate subcor-

tical visual areas, such as the thalamic nuclei, despite them being crucial for understanding the visual system.

The lateral geniculate nucleus (LGN) is a key thalamic nucleus in the human visual system (Livingstone and Hubel, 1988; Bakken et al., 2021). It is widely known that the LGN receives visual inputs from retinal ganglion cells and transfers those signals to the primary visual cortex (Nassi and Callaway, 2009). While the role of the LGN in transmitting visual signals has been extensively studied (Livingstone and Hubel, 1988), other lines of research suggest that the LGN is involved in a wide range of visual functions, including eye-specific dominance and suppression during binocular rivalry (Haynes et al., 2005), visual

* Corresponding author at: Center for Information and Neural Networks (CiNet), Advanced ICT Research Institute, National Institute of Information and Communications Technology, Suita 565-0871, Japan.

E-mail addresses: hoishi@berkeley.edu (H. Oishi), htakemur@nips.ac.jp (H. Takemura).

<https://doi.org/10.1016/j.neuroimage.2022.119777>.

Received 8 March 2022; Received in revised form 26 November 2022; Accepted 29 November 2022

Available online 30 November 2022.

1053-8119/© 2022 The Author(s). Published by Elsevier Inc. This is an open access article under the CC BY license (<http://creativecommons.org/licenses/by/4.0/>)

attention (O'Connor et al., 2002; Schneider and Kastner, 2009; Ling et al., 2015), and visual perceptual learning (Yu et al., 2016). The LGN is also involved in the neuronal synchrony widely observed in the visual cortex (Hughes et al., 2004; Liu et al., 2012; Minami et al., 2020). Understanding the structure and function of the LGN is also essential for evaluating morphological degeneration related to diseases (Mcketton et al., 2014; Giraldo-Chica and Schneider, 2018) and the anatomical basis of residual visual functions in blindsight (Schmid et al., 2010; Bridge et al., 2019; Atapour et al., 2021).

The human LGN is composed of six layers that are categorized into two major subdivisions: the magnocellular (M) and parvocellular (P) subdivisions. These subdivisions are clearly distinguishable on the basis of cell size, with larger neurons in the M subdivision than the P subdivision (Hickey and Guillery, 1979; Gupta et al., 2006). A number of studies have suggested that the M and P subdivisions have complementary roles in visual processing by demonstrating distinct spatial, temporal, luminance, and chromatic stimuli preferences (Derrington and Lennie, 1984; Schiller et al., 1990; Usrey et al., 2000; Denison et al., 2014). According to psychophysical performances in response to specific types of visual stimuli and neural responses in the M and P subdivisions, these two subdivisions have been proposed to have distinct roles in attention (Yeshurun and Levy, 2003) and reading (Demb et al., 1998; Stein, 2001; Main et al., 2014). A psychophysical study using a motion coherence task also led to a hypothesis that the M subdivision is damaged earlier than the P subdivision as a consequence of glaucoma (Joffe et al., 1997). However, the hypotheses proposed by previous psychophysical studies remain speculative because they are derived mostly from similarities between the neural responses of the M and P subdivisions and stimuli-dependent psychophysical performances without assessing the differences in functional and structural measurements between the two. Therefore, it is essential to establish a method to identify LGN subdivisions in individual living human brains to enable the direct comparison of neuroimaging data from the LGN subdivisions and psychophysical data.

Non-invasive neuroimaging-based measurements of the structural properties of human LGN subdivisions have been challenging because of the requirements of high-resolution and quantitative magnetic resonance imaging (MRI) measurements for the LGN, which has a small volume of approximately 180 mm³ (Mcketton et al., 2014). Several neuroimaging approaches to identify LGN subdivisions have been proposed. The first approach is to use functional MRI (fMRI) to localize M and P subdivisions based on the difference in blood oxygenation level-dependent (BOLD) response selectivity for distinct visual stimuli. While previous studies successfully demonstrated the utility of fMRI to identify human LGN subdivisions (Denison et al., 2014; Zhang et al., 2015, 2016), this approach has some limitations regarding the spatial resolution (1.25–2 mm isotropic voxels), robustness of the measurements, and necessity of the use of visual stimuli, which limits the applicability for clinical populations with visual field loss. The second approach is to use quantitative structural MRI to identify LGN subdivisions based on tissue differences between them. By using 7T MRI, Müller-Axt et al. (2021) demonstrated that this approach enables them to identify human LGN subdivisions using high-resolution measurements performed on *ex vivo* human brains. They also identified LGN subdivisions in individual human brains *in vivo*, using the LGN population atlas averaged across subjects as a common reference space. However, structural MRI-based identification of the LGN subdivisions in living humans using clinically feasible 3T MRI remains to be achieved.

Macromolecular tissue volume (MTV) is a promising quantitative structural MRI method that has been proven to be highly correlated with lipid volume fraction. It provides consistent results across hardware, enabling more quantitative comparisons across brain regions and subjects (Mezer et al., 2013). We expected that non-invasive MTV measurements using 3T MRI would be useful for identifying M and P subdivisions, each of which has different microstructural properties in both cellular and subdivision scales. Specifically, while the cell size of M neurons is

larger than that of P neurons, the M and P subdivisions also have different structural characteristics at the subdivision scale, such as higher neuronal cell densities and greater myelin densities in the P subdivision than in the M subdivision in non-human primates (Hassler, 1966; Yücel et al., 2000, 2003; Pistorio et al., 2006) and in humans (Müller-Axt et al., 2021). Because MTV is a measurement at the millimeter scale and will mainly represent anatomical characteristics at the subdivision level, the P subdivision might show a higher MTV than the M subdivision. Here, we examined whether the M and P subdivisions could be distinguished by the MTV in individual living humans.

Using our newly developed method, we found a gradual change in the MTV fraction within the LGN along each axis (lateral–medial, ventral–dorsal, and anterior–posterior). This pattern of change was consistent among subjects and enabled the parcellation of the LGN into two subdivisions in a consistent manner with post-mortem human data. Moreover, the difference in stimulus selectivity of the BOLD response between the subdivisions identified by MTV was consistent with previous physiological studies. The MTV-based LGN parcellation was robust over measurements taken on different days. The parcellation using widely used non-quantitative methods such as the T1-weighted/T2-weighted (T1w/T2w) ratio map was less accurate, which suggested that quantitative structural mapping is crucial for identifying the M and P subdivisions in human LGN. This study provides a novel method of non-invasively investigating the properties of LGN subdivisions in living human brains, which can be combined with functional or behavioral experiments to test neuroscientific or clinical hypotheses.

2. Materials and methods

The first step in our proposed method was to identify the location and contour of the entire LGN using high-resolution proton density (PD)-weighted imaging, as employed in previous studies of human LGN (Mcketton et al., 2014; Viviano and Schneider, 2015; Giraldo-Chica and Schneider, 2018). We then defined the LGN subdivisions using the MTV fraction data and the anatomically known volume ratio of the M and P subdivisions. Finally, we tested the validity of the definition based on (1) comparisons with histological data, (2) fMRI measurements of stimulus selectivity, and (3) an analysis of test-retest reliability.

2.1. Subjects

Fifteen healthy volunteers (7 females; mean age, 23.53 years; standard deviation, 1.71 years; range, 21–26 years) participated in this study. All subjects had normal or corrected-to-normal vision with no clinical history of eye disease. None of the subjects had a history of neurological disorders. All subjects provided written informed consent to participate in this study. The study was conducted in accordance with the ethical standards of the Declaration of Helsinki and approved by the local ethics and safety committees of the Center for Information and Neural Networks (CiNet), Advanced ICT Research Institute, National Institute of Information and Communications Technology.

The main analysis performed in this study was a single-subject approach focused on the identification of LGN subdivisions in individual subjects, visual inspection of results in each subject, and comparisons among the subject data and histological data without performing statistical tests of group differences. Therefore, statistical power and sample size estimation are not relevant for these analyses. For some analyses, we performed statistical tests to evaluate differences between M and P subdivisions using the two-tailed paired *t*-test (e.g. Fig. 4, Fig. 6). We expected a large effect size ($d' > 1.10$) in the fMRI experiment, considering the large separation effect reported in a previous fMRI work (Denison et al., 2014). The power of this study ($N = 15$) was sufficiently larger than the sample size required to detect a large effect ($d' = 1.10$) in the power analysis using a two-tailed paired *t*-test ($N = 13$; G*Power 3.1).

2.2. Structural MRI data acquisition

All MRI data were collected at the CiNet using a 3T MAGNETOM SIEMENS Prisma scanner (Siemens Healthcare, Erlangen, Germany) with a 32-channel head coil.

2.2.1. T1w MRI data acquisition

T1w magnetization prepared-rapid gradient echo (MPRAGE) images (voxel size, 0.75 mm \times 0.75 mm \times 1.0 mm; repetition time [TR], 1900 ms; echo time [TE], 3.58 ms; flip angle, 9°; matrix, 256 \times 256 \times 208; in-plane acceleration factor, 2) were acquired from all subjects. These images were used as references, on which the subsequent MRI data (PD-weighted, MTV, T1w/T2w ratio and fMRI data) was coregistered in the same coordinate space for each individual subject. The total acquisition time for the T1w MRI data was approximately 15 min per subject.

2.2.2. PD-weighted MRI data acquisition

PD-weighted images were acquired from all subjects to locate the LGN. The acquisition parameters of the PD-weighted images were the same as those used in a previous study of the human LGN (Viviano and Schneider, 2015; voxel size, 0.75 mm \times 0.75 mm \times 1.0 mm; TR, 3000 ms; TE, 21.0 ms; flip angle, 120°; matrix, 256 \times 256; in-plane acceleration factor, 2). These images were acquired at least 40 times in all subjects. To improve the signal-to-noise ratio, we continued to repeat the PD-weighted image acquisition if the subjects agreed (maximum number of repetitions: 60). Each image consisted of 50–60 coronal slices (slice thickness, 1 mm; no gap) covering the whole posterior thalamus. The total acquisition time for the PD-weighted MRI data was approximately 60–90 min per subject, depending on the number of repetitions.

2.2.3. MTV data acquisition

The MTV data were acquired from all subjects according to a previously described protocol (Mezer et al., 2013; Oishi et al., 2018; Takemura et al., 2019; Minami et al., 2020). In brief, four fast low-angle shot (FLASH) images were measured with flip angles of 4°, 10°, 20°, and 30° (TR, 12 ms; TE, 2.43 ms) with 1 mm isotropic voxels. We used a short TE, as used in the original works proposing the use of MTV to minimize T2* (Mezer et al., 2013, 2016). For the purposes of removing field inhomogeneities, five additional spin echo inversion recovery (SEIR) scans were also measured with an echo planar imaging (EPI) readout (TR, 3 s; TE, 49 ms; 2 \times acceleration). The inversion times were 50, 200, 400, 1200, and 2400 ms. The in-plane resolution and slice thickness of the additional scan were 2 mm \times 2 mm \times 4 mm, respectively. The total acquisition time for MTV data was approximately 35 min per subject. For 13 subjects, we acquired MTV data again on a different day to evaluate the test–retest reproducibility.

2.2.4. T1w/T2w MRI data acquisition

We also acquired data from 13 subjects for a T1w/T2w ratio map, a technique widely used in the analysis of Human Connectome Project data (Glasser and Van Essen, 2011). The T1w image was acquired using a 3D MPRAGE (TR, 2400 ms; TE, 2.06 ms; TI, 1000 ms; flip angle, 8°; bandwidth, 220 Hz/pixel; echo spacing, 7.5 ms; matrix, 256 \times 256 \times 176; voxel size, 1 mm isotropic resolution) sequence. The T2w image was acquired using sampling perfection with application optimized contrast using different angle evolutions (SPACE: TR, 3200 ms; TE, 438 ms; flip angle, 120°; bandwidth, 574 Hz/pixel; echo spacing, 3.88 ms; turbo factor, 139; matrix, 256 \times 256 \times 176; voxel size, 1 mm isotropic resolution) sequence. The T1w image acquired for T1w/T2w is distinct from the T1w image used for the main analysis which have different in-plane voxel size (see 2.2.1 T1w MRI data acquisition). Although these acquisition protocols aimed to follow those used in the Human Connectome Project (Glasser and Van Essen, 2011), they were not identical due to hardware differences. These data were collected using prescan normalization to reduce image intensity bias.

2.3. Structural MRI data analysis

2.3.1. T1w MRI data

The T1w MRI images of individual subjects were interpolated and aligned to the ICBM 152 2009b symmetric template in the MNI152 database (Fonov et al., 2009, 2011; <http://www.bic.mni.mcgill.ca/ServicesAtlases/ICBM152Nlin2009>; voxel size, 0.5 mm isotropic resolution) using a rigid-body transformation implemented in the FSL FLIRT tool (Jenkinson et al., 2002). No spatial smoothing or normalization was performed. These T1w MRI images of individual subjects in MNI space were used for coregistration with PD-weighted, MTV, T1w/T2w ratio and fMRI data to enable comparisons among datasets in MNI coordinate space. T1w MRI images were also used for the segmentation of the gray and white matter, thalamus, pallidum, and putamen. Segmentation was performed using the FAST and FIRST tools in FSL (Zhang et al., 2001; Patenaude et al., 2011).

2.3.2. PD-weighted MRI data

The PD-weighted image from the first scanning session was used as a reference. All subsequent PD images acquired from the same subject were coregistered to the reference using a rigid-body transformation implemented using the FSL FLIRT tool. We then averaged all PD-weighted images. The averaged PD-weighted image was then interpolated and aligned to the T1w MRI data in MNI coordinate space.

2.3.3. MTV data

Using the mrQ software package (<https://github.com/mezera/mrQ>) in MATLAB, the FLASH and SEIR scans were processed to produce the MTV maps (Mezer et al., 2013, 2016). MTV aims to quantify the microstructural properties of brain tissue based upon the non-water volume fraction. To this end, the mrQ pipeline first calculates the PD value in each voxel based on the FLASH data acquired with multiple flip angles (Mezer et al., 2016). The PD map is then corrected for inhomogeneity of the radiofrequency transmit and gains of receiving coils. The former inhomogeneity is corrected by using the unbiased field map derived from the SEIR-EPI scans (Barral et al., 2010). The latter one is corrected by combining FLASH data from individual coils with different gains (Mezer et al., 2013). Note that the SEIR-EPI images were coregistered with FLASH images using Advanced Normalization Tools (ANTs, <http://stnava.github.io/ANTs/>) included in the mrQ pipeline, and we visually confirmed that ANTs registration successfully coregistered the SEIR-EPI images with some distortion into FLASH images for all subjects. Lastly, the mrQ pipeline calculates the MTV map based on the bias-corrected PD maps. The mrQ pipeline uses voxels in the cerebrospinal fluid (CSF) as a reference, as these voxels are fully filled with water (water volume fraction [WVF] = 1.00) regardless of the subject and MR hardware. The mrQ pipelines defined the CSF voxels as voxels in which T1 relaxation time is approximately 4.3 s, a value known as the T1 of the ventricle. The MTV is defined as follows: $MTV = 1 - WVF$, which is used to quantify the non-proton macromolecule volume fraction in each voxel. Following calibration using CSF voxels, MTV has been proven to be consistent across MR hardware (Mezer et al., 2013). We note that some voxels within the ventricle have non-zero MTV fractions, since those voxels are not classified as CSF voxels in the mrQ pipeline. Those voxels do not show T1 close to 4.3 s due to measurement noise or the presence of the choroid plexus. Finally, the MTV map is aligned to the T1w MRI data to enable further comparisons with other images in the same coordinate space. The full analysis pipeline and validation results for the MTV method can be found in previous publications (Mezer et al., 2013, 2016; Oishi et al., 2018; Takemura et al., 2019; Minami et al., 2020). The code for calculating MTV is publicly available (<https://github.com/mezera/mrQ>).

2.3.4. T1w/T2w MRI data

We obtained a T1w/T2w ratio map by coregistering the T2w image to the T1w image using the FLIRT tool in the FSL using rigid-body trans-

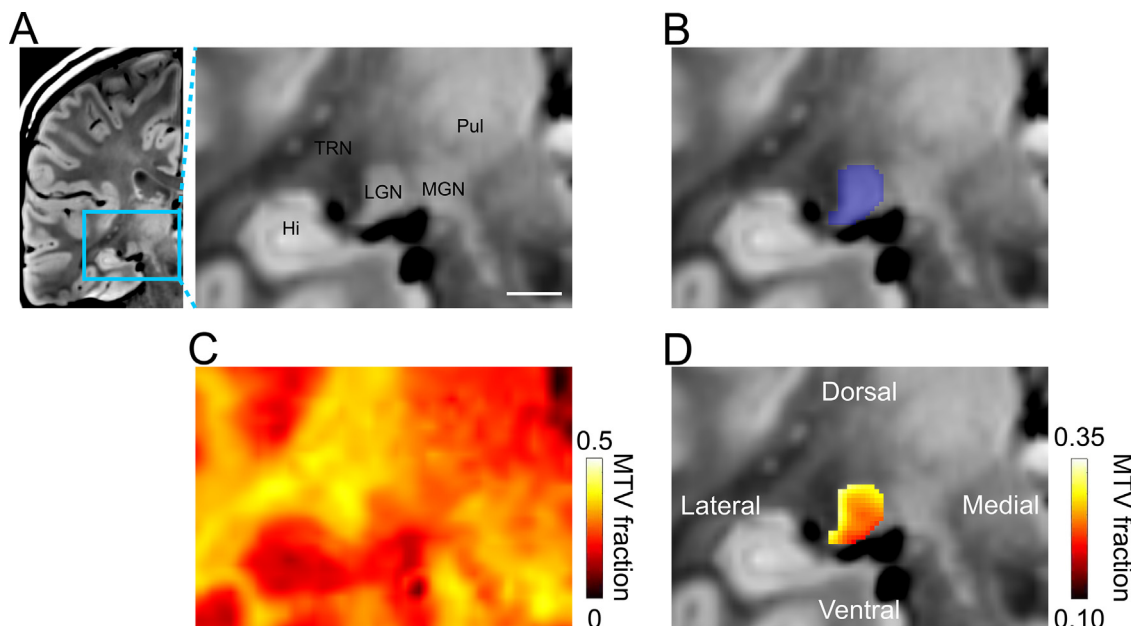


Fig. 1. The identification of whole lateral geniculate nucleus (LGN) and macromolecular tissue volume (MTV) mapping in the LGN of a single human subject. (A) A coronal section of a proton-density (PD) weighted image in a representative subject (left hemisphere, Subject S10). *Left panel*, the coronal PD-weighted image of the whole left hemisphere. The cyan rectangle indicates the region magnified in the right panel. *Right panel*, the magnified PD-weighted image near the LGN. TRN, thalamic reticular nucleus; Hi, hippocampus; MGN, medial geniculate nucleus; Pul, pulvinar. The scale bar (white line) indicates 6 mm. (B) The region-of-interest (ROI) covering the whole LGN (translucent blue), which was manually defined from the PD-weighted image. (C) MTV map coregistered with the PD-weighted image. The hot color map corresponds to MTV fractions in individual voxels. The MTV image has a lower resolution than the PD-weighted image because of a larger voxel size (1 mm isotropic). Additionally, some voxels within the ventricle have non-zero MTV fractions since the mrQ pipeline has rigorous criteria for selecting CSF voxels based on T1 relaxation time (see Materials and Methods). (D) MTV fractions within the LGN ROI. The MTV fraction gradually changed along the ventral–dorsal and lateral–medial axes. Note that the scale of the MTV fraction differs from that of panel C.

formation and calculated the ratio between them. The T1w/T2w ratio map was then coregistered to the reference T1w MRI data in the MNI coordinate space.

2.4. Identifying LGN from PD-weighted MRI data

We identified the position of the LGN in individual subjects based on the PD-weighted image averaged across multiple acquisitions (Fig. 1). This is because a previous study (Viviano and Schneider, 2015) demonstrated that the averaged PD-weighted image has good contrast in identifying the LGN. Following the procedure described by Viviano and Schneider (2015), the entire LGN was manually delineated based on visible intensity differences between the LGN and neighboring tissues (surrounding white matter and CSF) using the ITK-snap tool (<http://www.itksnap.org/>; Fig. 1B). Delineation was performed by two raters who were blinded to the purpose of this study. We primarily used the delineation of the first rater for the main analysis, and the delineation of the second rater was used to confirm inter-rater consistency. Delineation was performed in a series of coronal sections of PD-weighted images, because the coronal sections had the highest spatial resolution compared with the axial and sagittal sections. The whole LGN region-of-interest (ROI) was used in subsequent analyses to classify the M and P subdivisions using MTV.

2.5. Parcellation of the LGN based on MTV and other structural MRI maps

2.5.1. Main analysis using the fixed volume ratio and MTV fractions

We first rank-ordered all of the voxels within the whole LGN ROI based on their MTV fractions. Previous phantom experiments confirmed that MTV measurements correlate with the lipid fraction (Mezer et al., 2013; Filo et al., 2019; Shtangel and Mezer, 2020). Previous histological studies have identified that the P subdivision has a higher neuronal cell density (Hassler, 1966; Yücel et al., 2000, 2003; Müller-Axt et al., 2021)

and greater myelin content (Pistorio et al., 2006; Müller-Axt et al., 2021) than the M subdivision. Therefore, we hypothesized that the P subdivision would demonstrate larger MTV fractions than the M subdivision. Hence, we classified the 20% of voxels with the lowest MTV fraction as the putative M subdivision and the remaining 80% of voxels as the putative P subdivision (Fig. 2 and Supplementary Figs. S1 and S2). This ratio was based on previously reported volumes of the LGN subdivisions from human histological studies (Andrews et al., 1997; Selemon and Begovic, 2007) and was used in a previous fMRI study (Denison et al., 2014). Fig. 2B provides examples of MTV-based LGN parcellation in a representative hemisphere.

2.5.2. LGN parcellation using PD-weighted image and T1w/T2w ratio map

We attempted to parcellate the LGN based on the image intensity of the non-quantitative structural MRI maps (PD-weighted image and T1w/T2w ratio map). For the PD-weighted image, we classified the 20% of voxels with the highest image intensity as the putative M subdivision and the remaining 80% of voxels as the putative P subdivision because the image contrast of PD-weighted images demonstrates an opposite trend to that of MTV maps. For the T1w/T2w ratio map, we used identical criteria as employed for the MTV mapping.

2.6. Histological data (BigBrain) analysis

To compare the MTV-based parcellation of the LGN subdivisions with the histological definition, we analyzed publicly available BigBrain data (100 μm version of the BigBrain 3-D Volume Data Release 2015 in MNI space from <https://bigbrain.loris.ca/>; Amunts et al., 2013). In brief, BigBrain is a 3D reconstruction of 7404 histological sections of one post-mortem human brain that provides high-resolution anatomical data aligned with MNI coordinate space. In this database, all six layers in the human LGN are visible (see Fig. 2C, Supplementary Fig. S3).

Manual segmentation of the M (layers 1–2) and P subdivisions (layers 3–6) of the human LGN was carried out on the BigBrain data. Manual

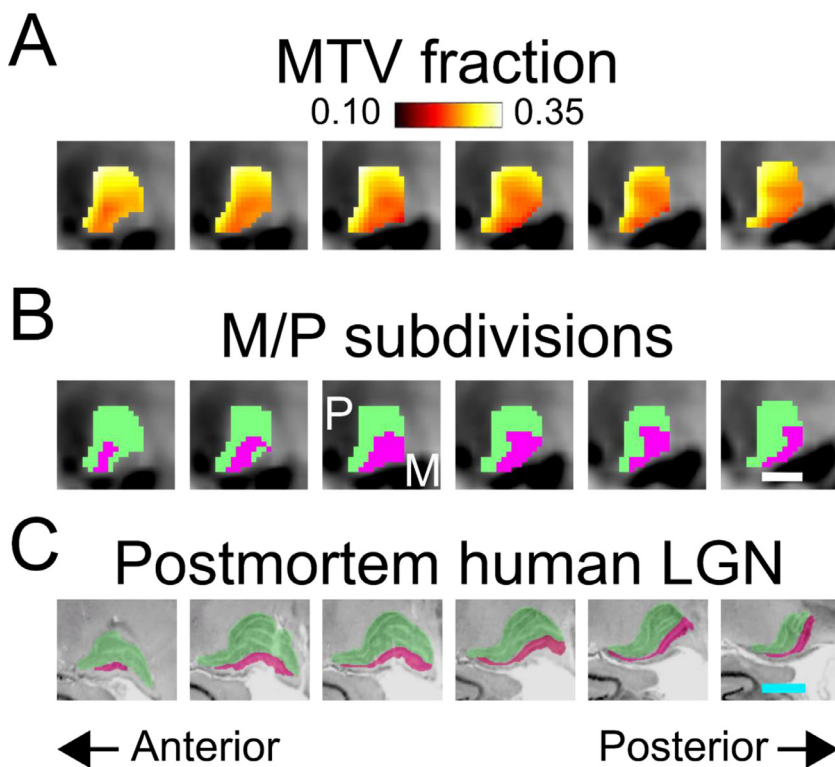


Fig. 2. LGN subdivisions parcellated by MTV fraction on a series of representative coronal sections in the LGN of a single human subject. (A) MTV fractions in the LGN ROI overlaid on a representative series of coronal sections of a PD-weighted image (the left and right panels represent anterior and posterior sections; distance between sections: 0.5 mm) in a representative hemisphere (left hemisphere, subject S10). The conventions were identical to those used in Fig. 1D. (B) The M and P subdivisions estimated from the MTV fractions in the hemisphere shown in panel A. We classified 20% of voxels with the lowest MTV fractions as belonging to the M subdivision (dark magenta) and the remaining 80% of voxels as belonging to the P subdivision (light green). The white scale bar indicates 4 mm. See Supplementary Figs. S1 and S2 for LGN images of all coronal sections in the left and right hemispheres, respectively. (C) The M and P subdivisions from a human histological dataset (BigBrain; Amunts et al., 2013). The cyan scale bar indicates 4 mm. See Supplementary Fig. S3 for LGN images of all coronal sections of the BigBrain data.

segmentation was performed by two raters (see 2.4 “Identifying LGN from PD-weighted MRI data”). We used the M and P subdivision definition from BigBrain as a reference to compare the MRI-based parcellation. The delineation performed by the first rater was used for the main analysis, whereas delineation performed by the second rater was used to evaluate inter-rater consistency. Manual segmentation of the BigBrain data is shown in Fig. 2C and Supplementary Fig. S3.

2.7. Comparison of MRI-based parcellation with histological data

To quantify the spatial organization of the M and P subdivisions, we calculated the spatial centers of both subdivisions in MRI and histological data, following the analysis used in a previous fMRI study (Denison et al., 2014). The 3D spatial centers of the M and P subdivisions were defined as the mean voxel coordinates in each spatial dimension (left–right, ventral–dorsal, and anterior–posterior) in MNI space. When coregistering the reference (T1w) image to MNI space, the human thalamic nuclei showed individual differences in their positions, volume, and shape (Csernansky et al., 2004). Therefore, the position of the LGN and its subdivision in the MNI coordinates is variable among individual brains. Thus, we calculated the relative position of the center of each LGN subdivision with respect to the widths of the LGN in each spatial dimension to compare the spatial organizations of LGN subdivisions between the datasets.

We also evaluated the degree of similarity between MRI-based parcellation (MTV, PD-weighted, and T1w/T2w ratio) and BigBrain data by calculating the cosine similarity of vectors connecting the spatial centers of the M and P subdivisions. We performed this comparison focusing on the vector orientation in two-dimensional space corresponding to coronal space (left–right; ventral–dorsal) because the data in this dimension have the highest spatial precision in both the PD-weighted images and BigBrain data.

2.8. Functional MRI data acquisition

All subjects took part in an additional fMRI experiment to investigate the stimulus selectivity of the BOLD response in LGN voxels. We

acquired fMRI data with 1.5 mm isotropic voxels for 10 subjects (S1–S10) and 2 mm isotropic voxels for 5 subjects (S11–S15).

2.8.1. Acquisition parameters

The fMRI data were acquired with an interleaved T2* weighted gradient echo sequence at voxel sizes of 1.5 or 2.0 mm isotropic using simultaneous multi-slice EPI sequences (TR, 2250 ms; TE, 40 ms; flip angle, 75°; in-plane field of view, 192 mm × 192 mm) provided by the Center for Magnetic Resonance Research, Department of Radiology, University of Minnesota (<https://www.cmrr.umn.edu/multiband/>; Moeller et al., 2010). Transverse axial slices (57 slices for 1.5 mm isotropic voxels and 50 slices for 2.0 mm isotropic voxels) with no gaps were oriented to cover the LGN and occipital lobe. Certain parameters differed for the acquisition of 1.5-mm and 2-mm isotropic voxel size data (multi-band factor, 3; acquisition matrix, 128 × 128; echo spacing, 0.93 ms; partial Fourier, 6/8 for 1.5 mm isotropic voxels; multi-band factor, 2; acquisition matrix, 96 × 96; echo spacing, 0.68 ms; partial Fourier was not applied for 2 mm isotropic voxels), while the other parameters were identical.

2.8.2. Stimuli, block design, and task

All visual stimuli were generated using Psychtoolbox 3 in MATLAB (<http://psychtoolbox.org/>). Stimuli were projected from a projector (WUX5000, Cannon, Tokyo, Japan) located outside the scanner room and reflected via a mirror onto a gamma-corrected translucent screen positioned over the subject’s head. Gamma-correction was applied using Mcalibrator2 (Ban and Yamamoto, 2013; <https://github.com/hiroshiban/Mcalibrator2>). Stimuli were presented on a full flat screen (416 mm × 222 mm) at a spatial resolution of 1920 × 1200 and a frame rate of 60 Hz. The screen was viewed via a mirror mounted over the subject’s eyes. The viewing distance and visual angle of the screen was 92 cm and 41.2° × 25.8°, respectively.

We adapted two types of publicly available stimuli (M-type and P-type stimuli; Fig. 4A) designed to elicit selective BOLD responses in the M and P subdivisions (Denison et al., 2014; <https://github.com/racheldenisov/MPLocalizer>). The M-type stimulus was a 100% contrast, black–white grating with a low spatial frequency (0.5 cycles per degree)

and higher flicker frequency (15 Hz). The P-type stimulus was a near-isoluminant red–green grating with higher spatial frequency (2 cycles per degree) and lower flicker frequency (5 Hz). The orientation of the grating (0°, 30°, 60°, 90°, 120°, or 150°) was changed every 3 s in a random manner. Prior to the fMRI experiment, we adjusted the luminance of the P-type stimuli to make it perceptually isoluminant using a flicker method (Ives, 1912; Minami and Amano, 2017).

We used a block design for the fMRI experiment in which each run comprised 15 blocks (6 blocks for each of the M- and P-type stimuli and 3 blocks with a blank screen). Each block was 20.25 s in duration (including 18 s for stimulus presentation and 2.25 s for the blank period, during which the subjects provided their responses). During each block, subjects were instructed to count the number of randomly presented targets, two-dimensional Gaussian contrast decrements within the stimuli, while maintaining fixation. A number of targets appeared during each block varied from 0 to 3. During the blank period, subjects reported how many targets they had seen during the previous stimulus block by pressing a button out of four buttons (see Supplementary Materials for the task performance results in the fMRI experiment). The subjects completed 7–8 runs. This procedure and other details of the stimuli, task, and block design have been previously described (Denison et al., 2014).

2.9. Functional MRI data analysis

The fMRI data were analyzed using mrVista (<https://github.com/vistalab/vistasoft>). We registered the data onto T1w MRI data to enable comparisons with other MRI datasets. We corrected the slice timing to match the multi-slice acquisition order. The data were then corrected for the subject's motion within and between scans. We fitted a general linear model consisting of predictors (M- and P-type stimuli were regressors) convolved with the hemodynamic response function (Boynton et al., 1996) to the time course of each voxel. We used the Boynton hemodynamic response function (HRF) to match the procedure in a previous fMRI study (Denison et al., 2014). By fitting the HRF model to the time series of BOLD responses, we estimated the beta values for the M- and P-type stimuli. We then calculated the difference between them (β_{M-P}) as follows:

$$\beta_{M-P} = \beta_{M-P} - \beta_{P-P} \quad (1)$$

We used β_{M-P} as an index for evaluating the stimulus selectivity of the LGN subdivisions identified by MTV. Since it is unlikely that physiological artifacts on BOLD signals can be different across different types of visual stimulus presentation, this subtraction can minimize the physiological artifacts on BOLD responses. We averaged the β_{M-P} across all voxels in each LGN subdivision parcellated on the basis of MTV maps. Finally, we compared β_{M-P} between the MTV-based M and P subdivisions to evaluate the consistency between the stimulus selectivity of the BOLD responses and MTV-based parcellation of the LGN subdivisions.

2.10. Test–retest reliability analysis

To assess the reproducibility of the MTV measurements and MTV-based LGN parcellation, we remeasured MTV of 13 subjects (mean age, 23.85 years; 5 females). The data acquisition and analysis of MTV retest data were identical to those of the main experiment. We evaluated the reproducibility of the MTV measurements within the LGN by calculating the intraclass correlation coefficient (ICC) of voxels between the test and retest data. In addition, we quantified the reproducibility of the MTV-based LGN parcellation by calculating the proportion of LGN voxels classified into the same subdivisions using the test and retest data. We evaluated the statistical significance of this proportion by comparison with a null distribution, which was obtained by shuffling the labeling of the M and P voxels 10,000 times and calculating the distribution of the proportions of voxels classified into the same subdivisions using

the test and shuffled data. Lastly, we performed a comparison between the retest and BigBrain data using the same procedure as that used for the test data.

3. Results

We identified the whole LGN in individual subjects using PD-weighted images and then used MTV maps (Mezer et al., 2013) to identify the LGN subdivisions at the single-subject level in fifteen subjects. The validity of MTV-based parcellation of human LGN was evaluated by comparisons with histological data of a postmortem human brain (BigBrain; Amunts et al., 2013) and fMRI data collected from identical subjects. Furthermore, we tested the validity of LGN parcellation using data obtained from other types of structural MRI images. Finally, we evaluated the test–retest reliability of the MTV-based parcellation of the human LGN.

3.1. The LGN in PD-weighted images

In each individual hemisphere, the position and shape of the whole LGN was visible in the PD-weighted images (Fig. 1A) as reported previously (Viviano and Schneider, 2015). We asked raters to delineate the whole LGN in all individual hemispheres by manually inspecting the PD-weighted images (Fig. 1A,B; see Materials and Methods). Supplementary Fig. S4 depicts the volume of the whole LGN in all individual hemispheres. The LGN volume identified from manual delineation on BigBrain histological data (Amunts et al., 2013) and previous structural MRI studies (Mcketton et al., 2014; Giraldo-Chica and Schneider, 2018) are also shown in Supplementary Fig. S4.

We evaluated the consistency of LGN delineation between the two raters. Dice coefficients of the LGN delineation by the two raters based on PD-weighted images were 0.74 ± 0.005 and 0.78 ± 0.004 in the left and right hemispheres (mean and \pm S.E.M across subjects), respectively. Dice coefficients of the LGN delineation by the two raters based on BigBrain data were 0.90 and 0.90 in the left and right hemispheres, respectively. While the manual delineation of the LGN performed by the two raters was not identical, there was a large overlap between raters. In subsequent analyses, we used the LGN ROI delineated by the first rater for the main analysis, and the delineation of the second rater confirmed inter-rater consistency.

Among the 15 subjects tested in this study, the mean (\pm S.E.M.) volume of the whole LGN was $153.48 \text{ mm}^3 \pm 2.32 \text{ mm}^3$ and $158.40 \text{ mm}^3 \pm 1.83 \text{ mm}^3$ in the left and right hemispheres, respectively. The LGN volume manually identified from PD-weighted images was, on the whole, consistent with that obtained from BigBrain data (168.65 mm^3 and 162.37 mm^3 in the left and right hemispheres, respectively) and previous MRI studies using similar PD-weighted images (Supplementary Fig. S4; Mcketton et al., 2014; Giraldo-Chica and Schneider, 2018). The right LGN was marginally significantly larger than the left ($d' = 0.61$, $t_{14} = 2.14$, 95% confidence interval [CI] = $-0.02-9.87$, $p = 0.05$, two-tailed paired t -test). Notably, the M and P subdivisions could not be identified through visual inspection of the PD-weighted image.

3.2. Identification of M and P subdivisions using the MTV fraction

Next, we analyzed the MTV maps coregistered with the PD-weighted images for each individual subject (Fig. 1C). In brief, the MTV method aims to quantify macromolecular tissue density by quantifying the proton density based on structural MRI data acquired with different parameters. The measurement is then calibrated using voxels in the CSF, which are fully filled with water, as a reference (see Materials and Methods for details). We note that in the dataset acquired in this study, MTV has sufficient sensitivity to identify known microstructural differences between subcortical structures (see Supplementary Materials and Supplementary Fig. S5 for MTV difference between pallidum and putamen).

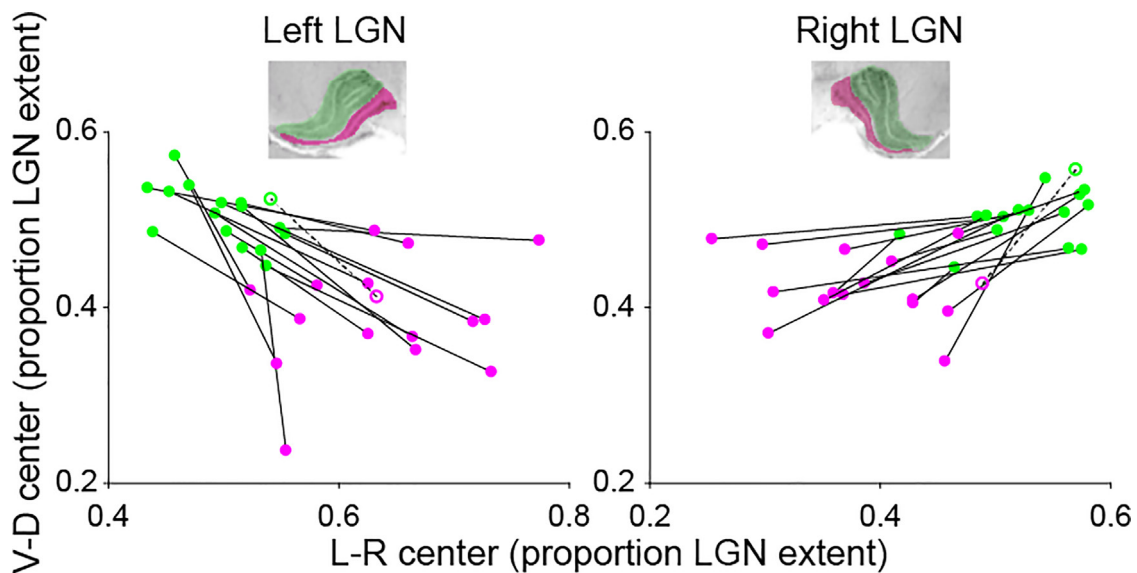


Fig. 3. Center positions of the MTV-based M and P subdivisions compared with BigBrain data. The panels depict the center positions for the M (magenta) and P subdivisions (green) in LGN (left panel, left LGN; right panel, right LGN). The horizontal and vertical axes represent the left–right and ventral–dorsal axes, respectively. The M and P subdivisions identified in a representative coronal slice using BigBrain data are inserted in each panel. The center positions were calculated in MNI coordinates and are plotted as a proportion of each subject’s entire LGN along a given axis. The filled circles and solid lines represent the spatial centers of the M and P subdivisions estimated from the MTV map in individual hemispheres. The open circles and dotted lines represent the spatial centers of the M and P subdivisions in a human histological dataset (BigBrain; Amunts et al., 2013). We found that the centers of the M voxels defined using the MTV were located more medially and ventrally than the P voxels in all hemispheres, which was consistent with the BigBrain histological data.

In all individual hemispheres, we observed gradual changes in MTV fractions within the LGN ROIs (Fig. 1D); the dorsal–lateral part of the LGN exhibited a higher MTV fraction than the ventral–medial part. We then parcellated the human LGN by incorporating prior knowledge from an anatomical study that demonstrated that the area of the P subdivision is roughly four times larger than that of the M subdivision (Andrews et al., 1997). Based on this knowledge, we classified 20% of the voxels with the lowest MTV as belonging to the putative M subdivision and the remaining 80% as belonging to the putative P subdivision (Fig. 2; see Supplementary Figs. S1 and S2 for results obtained from all subjects). We found that the voxels classified as part of the putative M subdivision appeared at the ventral–medial part, whereas those classified as part of the putative P subdivision appeared at the dorsal–lateral part. We also note that these M and P subdivisions were observed as two distinct clusters of voxels, which were highly continuous across slices in most hemispheres (Supplementary Figs. S1 and S2).

3.3. Validations of M and P subdivisions identified using MTV data

We evaluated the validity of the MTV-based LGN parcellation by comparing it with the publicly available histological data for human LGN subdivisions (BigBrain; Amunts et al., 2013; Supplementary Fig. S3). To do so, we calculated the centers of the coordinates among all of the M and P subdivision voxels classified based on the MTV in all hemispheres and compared them with those from the BigBrain data (Fig. 3 and Supplementary Fig. S6). Because voxels classified as belonging to the M or P subdivision mostly formed distinct clusters in each individual hemisphere (Supplementary Figs. S1 and S2), the spatial center was a valid metric for comparisons with histological data. In the BigBrain data, the center of the M subdivision was located in the medial, posterior, and ventral part of the LGN, while the center of the P division was located in the lateral, anterior, and dorsal part (dashed lines and open circles in Fig. 3, Supplementary Fig. S6). This spatial organization of M and P subdivisions was in line with the prior human histological LGN study (Selemon and Begovic, 2007). We found that the center of the coordinates for the M and P subdivisions defined by the *in vivo* MTV

data showed a similar trend as that seen using the BigBrain data, and this trend was well replicated across all subjects (solid lines and filled circles in Fig. 3, Supplementary Fig. S6). In addition, the M and P subdivisions estimated by MTV showed a pattern consistent with those of the BigBrain data when we used the LGN ROI delineated by a second rater (Supplementary Fig. S7). Therefore, these results suggest that the LGN subdivisions identified using the MTV were in good agreement with the anatomical architecture defined using histological human LGN data. We note that when we classify voxels based solely on position (ventral 20% of the voxels as the M subdivision; the remaining 80% as the P subdivision), we could not obtain parcellation consistent with the BigBrain data (Supplementary Fig. S8).

We also performed supplementary analyses to address how much results depend on the arbitrary choice of a fixed volume ratio between M and P subdivisions (Denison et al., 2014) by testing different ratios (Supplementary Fig. S9) or a fixed threshold value of MTV rather than fixed ratio between M and P subdivisions (Supplementary Fig. S10). The center of coordinates for the M and P subdivisions defined by both criteria were consistent with those of the BigBrain data (see Supplementary Materials).

3.4. MTV-based M and P subdivisions exhibited different visual stimulus selectivity on fMRI

In the above analysis, we tested the validity of our parcellation based on the spatial arrangement of the M and P subdivisions. We further tested whether the M and P subdivisions identified using MTV exhibited the different visual stimulus sensitivities reported in previous macaque and human studies. Specifically, the M subdivision is more sensitive to luminance contrast stimuli with lower spatial frequency and higher temporal frequency but is less sensitive to chromatic stimuli; the P subdivision is more sensitive to chromatic stimuli with higher spatial frequency and lower temporal frequency but is less sensitive to luminance contrast stimuli (Derrington and Lennie, 1984; Usrey et al., 2000; Denison et al., 2014; Zhang et al., 2015; Yu et al., 2016). Using fMRI, we measured the BOLD responses to a pair of visual stimuli designed to differentially

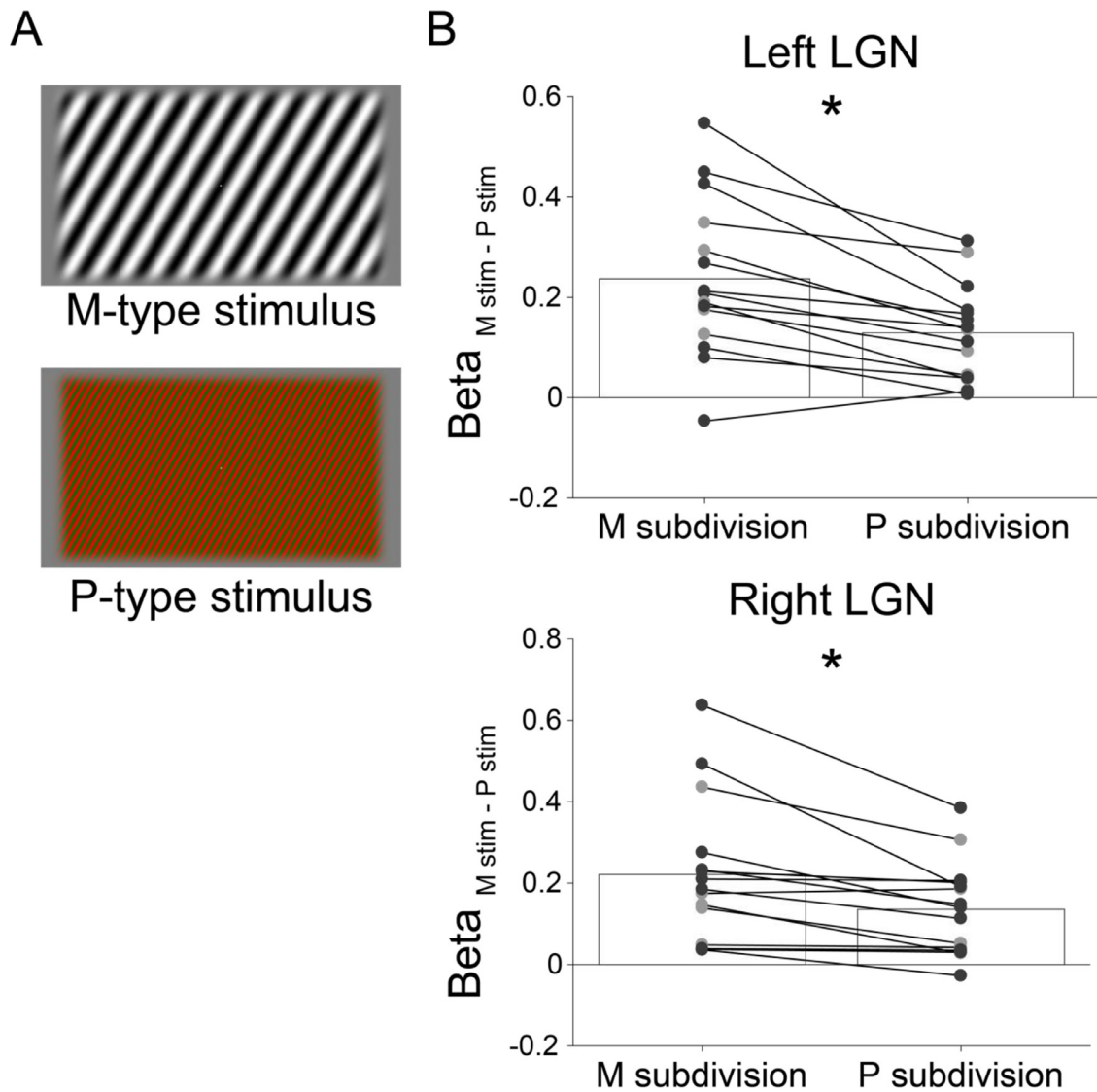


Fig. 4. MTV-based M and P subdivisions exhibit stimulus selectivity as reported in previous literature. (A) Stimuli used to test the functional selectivity of M and P subdivisions. *Upper panel:* An achromatic, low spatial, and high temporal frequency with high luminance contrast grating stimulus used to activate the M subdivision. *Lower panel:* A high color contrast, high spatial, and low temporal frequency with low luminance contrast grating stimulus used to activate the P subdivision. These stimuli were adapted from Denison et al. (2014). (B) Stimulus selectivity measured by fMRI in the MTV-based M and P subdivisions (*top panel*, left LGN; *bottom panel*, right LGN; $N = 15$ each). The vertical axis depicts the difference in the beta value between the M- and P-type stimuli (a positive value indicates higher sensitivity to M-type stimuli). The dots indicate data in individual hemispheres. The dark and light gray dots represent the measurements with 1.5 mm isotropic (S1–S10) and 2.0 mm isotropic (S11–S15) voxels, respectively. The asterisks represent statistically significant differences in stimulus selectivity between the M and P subdivisions measured using the BOLD response (two-tailed paired t -test, *: $p < 0.0005$). Details of the fMRI methods are described in *Materials and Methods, Functional MRI data acquisition*.

activate the M and P subdivisions (Fig. 4A; see Materials and Methods, Functional MRI data acquisition). We examined the extent to which the M and P subdivisions defined using MTV exhibited different stimulus selectivity in their BOLD response.

We calculated the difference in the beta weights of the M- and P-type stimuli ($\text{Beta}_{\text{Mstim-Pstim}}$; a positive value indicated that the BOLD response was greater for the M-type stimuli) for the M and P subdivisions defined using the MTV in individual hemispheres (Fig. 4B). A group analysis showed a significant difference in the $\text{Beta}_{\text{Mstim-Pstim}}$ between the M and P subdivisions ($d' = 0.84$, $t_{14} = 4.54$, $\text{CI} = 0.06\text{--}0.16$, $p = 0.0005$ for the left hemisphere; $d' = 0.57$, $t_{14} = 3.58$, $\text{CI} = 0.03\text{--}0.14$, $p = 0.003$ for the right hemisphere, two-tailed paired t -test). This consistency with known stimulus selectivity in the M and P subdivisions further supports the finding that MTV-based parcellation provides

reasonable *in vivo* identification of LGN subdivisions at the level of individual hemispheres.

3.6. Inter-subject variability in MTV fractions

We examined whether the MTV fractions in the estimated M and P subdivisions were consistent across the healthy subjects who participated in this study (Fig. 5). The MTV fractions of the estimated M subdivision were 0.25 ± 0.003 and 0.24 ± 0.004 for the left and right hemispheres (mean \pm S.E.M across subjects), respectively, whereas the MTV fractions of the estimated P subdivisions were 0.29 ± 0.003 and 0.28 ± 0.003 for the left and right hemispheres, respectively. Therefore, the inter-subject variability of the MTV fractions of each subdivision was much smaller than the mean difference between the M and P subdivi-

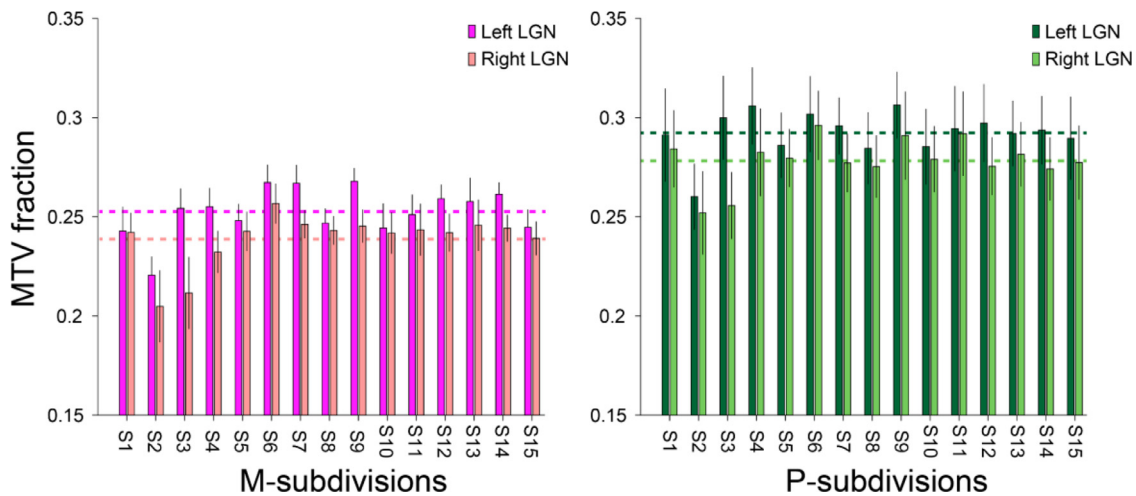


Fig. 5. MTV fractions in the estimated M and P subdivisions were similar across all subjects. The vertical axis depicts the MTV fraction averaged across voxels within the M (*left panel*, magenta) and P subdivisions (*right panel*, green) in individual hemispheres. The dark and light bars indicate the MTV fractions of the left and right hemispheres, respectively. The horizontal dotted lines indicate the averages for each hemisphere across subjects. The MTV fractions in each subdivision were similar across 15 subjects. The error bars depict ± 1 standard deviation across the voxels.

sions in healthy subjects. Given the low variability in the measurements across the healthy population, MTV measurements of the LGN are reliable for use in evaluating how the LGN tissue in patients with, for example, eye disease deviates from that of control subjects. We describe the inter-hemispheric differences in MTV of M and P subdivisions in the Supplementary Materials.

3.7. Parcellation using PD-weighted images and T1w/T2w ratio maps

MTV is a useful method for obtaining quantitative measurements of brain tissue properties (Mezer et al., 2013; Duval et al., 2017; Berman et al., 2018). However, a number of studies have used other types of MRI-based metrics, such as the ratio between T1w and T2w images (T1w/T2w ratio), to evaluate tissue properties. The acquisition time for these images is shorter, although the measurements are not fully quantitative (Glasser and Van Essen, 2011; Glasser et al., 2016). Therefore, we tested whether the M and P subdivisions can be similarly parcellated using image intensities on non-quantitative structural MRI scans to evaluate the potential advantages of the MTV-based approach.

We tested LGN parcellation using the intensities of the PD-weighted images (Fig. 6A), which were used to identify the whole LGN. Parcellation was also investigated using the T1w/T2w ratio map, which has often been used in previous studies to parcellate cortical areas (Fig. 6B; Glasser and Van Essen, 2011). We found that parcellation using the PD-weighted images and T1w/T2w ratio map appears to be less consistent with the BigBrain data in many cases (Fig. 6); this contrasts with the MTV-based parcellation (Fig. 3), in which the M subdivisions are located more medial and ventral than the P subdivisions in a consistent manner with the BigBrain data and a previous anatomical study (Selemon and Begovic, 2007).

We then quantified the degree of similarity between BigBrain and MRI-based parcellations (MTV, PD-weighted, and T1w/T2w) by calculating the cosine similarity of the vector connecting the spatial centers of M and P subdivisions with those of the BigBrain data (Fig. 6C; see Materials and Methods). In both hemispheres, MTV-based parcellation showed high similarity with BigBrain data (0.92 and 0.84 for left and right hemispheres, respectively). The cosine similarity of PD-weighted image-based parcellation was 0.30 and 0.58 for the left and right hemispheres, respectively, which was lower than that of MTV-based parcellation although this difference reached statistical significance only in the left hemisphere after Bonferroni correction ($d' = 2.92$, $t_{14} = 7.84$, $CI = 0.45\text{--}0.79$, $p = 0.00002$ for the left hemisphere; $d' = 0.92$,

$t_{14} = 2.46$, $CI = 0.03\text{--}0.49$, $p = 0.03$ for the right hemisphere, two-tailed paired t -test). The cosine similarity of the T1w/T2w ratio map-based parcellation for the left hemisphere was 0.79, which was significantly lower than that of the MTV-based parcellation ($d' = 1.23$, $t_{12} = 3.43$, $CI = 0.04\text{--}0.19$, $p = 0.005$, two-tailed paired t -test), whereas the cosine similarity of the T1w/T2w ratio map-based parcellation for the right hemisphere was 0.83, which was not significantly different from that of the MTV-based parcellation ($d' = 0.04$, $t_{12} = 0.07$, $CI = -0.11\text{--}0.12$, $p = 0.95$, two-tailed paired t -test). We note that while we did not find significant differences in the cosine similarity, the T1w/T2w ratio map-based parcellation in the right hemisphere appears to be inferior to the MTV-based parcellation in Fig. 6B. This is because in seven subjects, the position of M center was lateral to the position of P center unlike the spatial organization of the subdivisions in the BigBrain data (Fig. 6B).

While MTV is corrected for both radiofrequency transmitter (B_1^+) inhomogeneity and receive-coil gain biases (Mezer et al., 2013), the PD-weighted map was not corrected for these biases. The T1w/T2w ratio map has been proposed as a proxy of myelin content, but it is not explicitly corrected for B_1^+ inhomogeneity (Glasser and Van Essen, 2011; Shams et al., 2019). Therefore, the better parcellation using MTV than that using PD or T1w/T2w presumably originates from correction for these measurement biases.

3.8. Assessment of the partial volume effect as a potential confounder

Because the LGN is surrounded by white matter and CSF (Fig. 1), it is possible that the partial volume effect on these surrounding tissues may lead to bias in the MTV-based identification of the M and P subdivisions. To address this concern, we performed additional analyses excluding voxels within 1 mm (the resolution of MTV data) from the LGN surface to minimize the partial volume effect in the surrounding tissue. We found that the consistency with BigBrain was reduced in this analysis using the 1 mm criterion, such that 17 of 30 hemispheres showed the same trend as the BigBrain data (Supplementary Fig. S11A), suggesting that the partial volume effect may potentially influence the results. However, it is difficult to interpret the results of this analysis because this analysis removed a large proportion of voxels ($76.80\% \pm 0.46\%$ mean \pm S.E.M across subjects) from the LGN ROI, which will create challenges for stable parcellation, regardless of the partial volume effect.

We believe that the partial volume effect may not fully account for the successful MTV-based parcellation because fMRI analysis using LGN

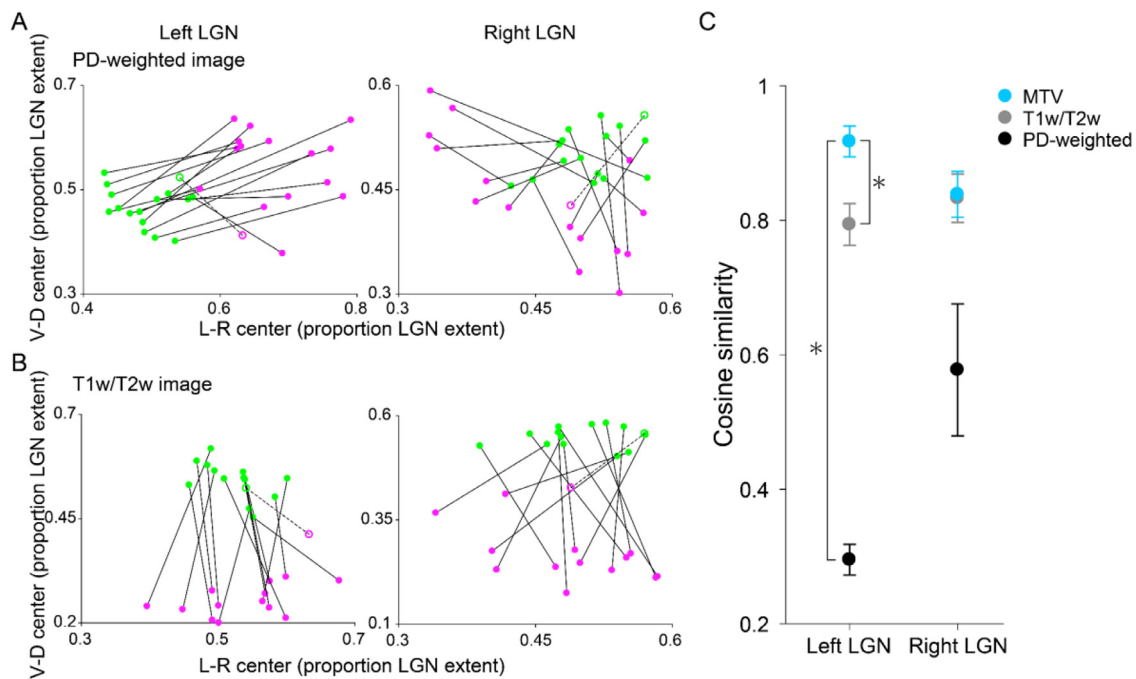


Fig. 6. LGN subdivisions may not be identifiable from non-quantitative structural MRI maps. (A) LGN parcellation based on the image intensities of PD-weighted images. The centers of the M and P voxels vary across the hemispheres and are inconsistent with the LGN coordinates obtained using the BigBrain data. (B) LGN parcellation based on the image intensities of T1w/T2w maps. In most hemispheres, the centers of the M and P voxels along the left–right axis are inconsistent with those of the BigBrain data. The conventions are identical to those used in Fig. 3. (C) Similarity of the vector connecting the spatial centers of the M and P subdivisions in the coronal plane (left–right and ventral–dorsal axes) between BigBrain and MRI-based parcellation (MTV, light blue; PD-weighted, black; T1w/T2w, gray). The asterisk indicates a statistically significant difference ($p < 0.025$, which is equal to $p = 0.05$ after Bonferroni correction for two comparisons). The error bars indicate ± 1 S.E.M.

ROI after the removal of LGN surface voxels showed that the difference in visual stimulus sensitivities between estimated M and P subdivisions was preserved despite removing voxels (Supplementary Fig. S11B; $d' = 0.69$, $t_{14} = 5.24$, CI = 0.06–0.14, $p = 0.0001$ for the left hemisphere; $d' = 0.23$, $t_{14} = 2.23$, CI = 0.002–0.08, $p = 0.04$ for the right hemisphere, two-tailed paired t -test). While the partial volume effect can be a potential confounder, it may not fully explain the successful MTV-based parcellation (see Discussion).

3.9. LGN M and P subdivisions were robust across sessions on different days

We tested the test–retest reliability of the M and P parcellations by performing the same MTV measurement in 13 subjects on a different day. The MTV fractions of voxels within the LGN ROI were highly correlated between the test and retest experiment (ICC(1,1) = 0.77; Fig. 7A; see Supplementary Fig. S12 for results in individual subjects, see Materials and Methods). In calculating the probability that individual voxels can be classified into the same subdivisions between the test and retest experiments, we demonstrated that 85.62% and 82.31% of voxels in the left and right LGN, respectively, were classified in the same subdivision (Fig. 7B; mean across subjects). To assess the statistical significance of these numbers, we randomly classified 80% of the voxels into the P subdivision and the remaining 20% into the M subdivision to obtain a null distribution. We repeated this process by shuffling the voxels 10,000 times. The maximum probabilities of the voxels being classified into the same subdivisions between the test and shuffled data were 71.73% and 71.55% for left and right hemispheres (mean across subjects), respectively, suggesting that the test–retest reliability of MTV-based parcellation was highly significant ($p < 0.0005$). Finally, using the retest dataset, we replicated the results indicating that the centers of the M and P subdivisions showed the same spatial patterns as in the histolog-

ical data (Fig. 7C; cosine similarity of MTV retest and BigBrain data, left = 0.93; right = 0.87). Taken together, these results support a considerable degree of reproducibility for our results from the MTV-based LGN parcellation.

4. Discussion

It is widely known that the human LGN consists of functionally and anatomically different subdivisions. However, identifying these subdivisions in individual living human brains using conventional structural neuroimaging methods had been challenging. In this study, we demonstrated the approximate parcellation of LGN subdivisions at the single-subject level by combining *in vivo* structural MRI methods (multiple PD-weighted imaging and MTV measurement). The spatial positions of the identified LGN subdivisions were consistent with those identified using histological data (Amunts et al., 2013). Furthermore, using fMRI, we confirmed that these subdivisions exhibit different stimulus selectivity, which is consistent with the findings of previous physiological studies. Finally, we confirmed that MTV-based LGN parcellation is highly consistent across datasets acquired on different days, suggesting that the proposed method is highly reproducible. Other non-quantitative structural MRI methods did not provide LGN parcellation consistent with histological data. Taken together, this study provides evidence of the utility of this quantitative structural MRI approach to LGN parcellation and establishes methods of measuring the structural properties of human LGN subdivisions in single living human subjects using a clinically feasible 3T MRI scanner.

4.1. Microstructural origin of MTV-based parcellation

Our results demonstrated that the MTV fraction can be a useful measurement for distinguishing M and P subdivisions. One might ask

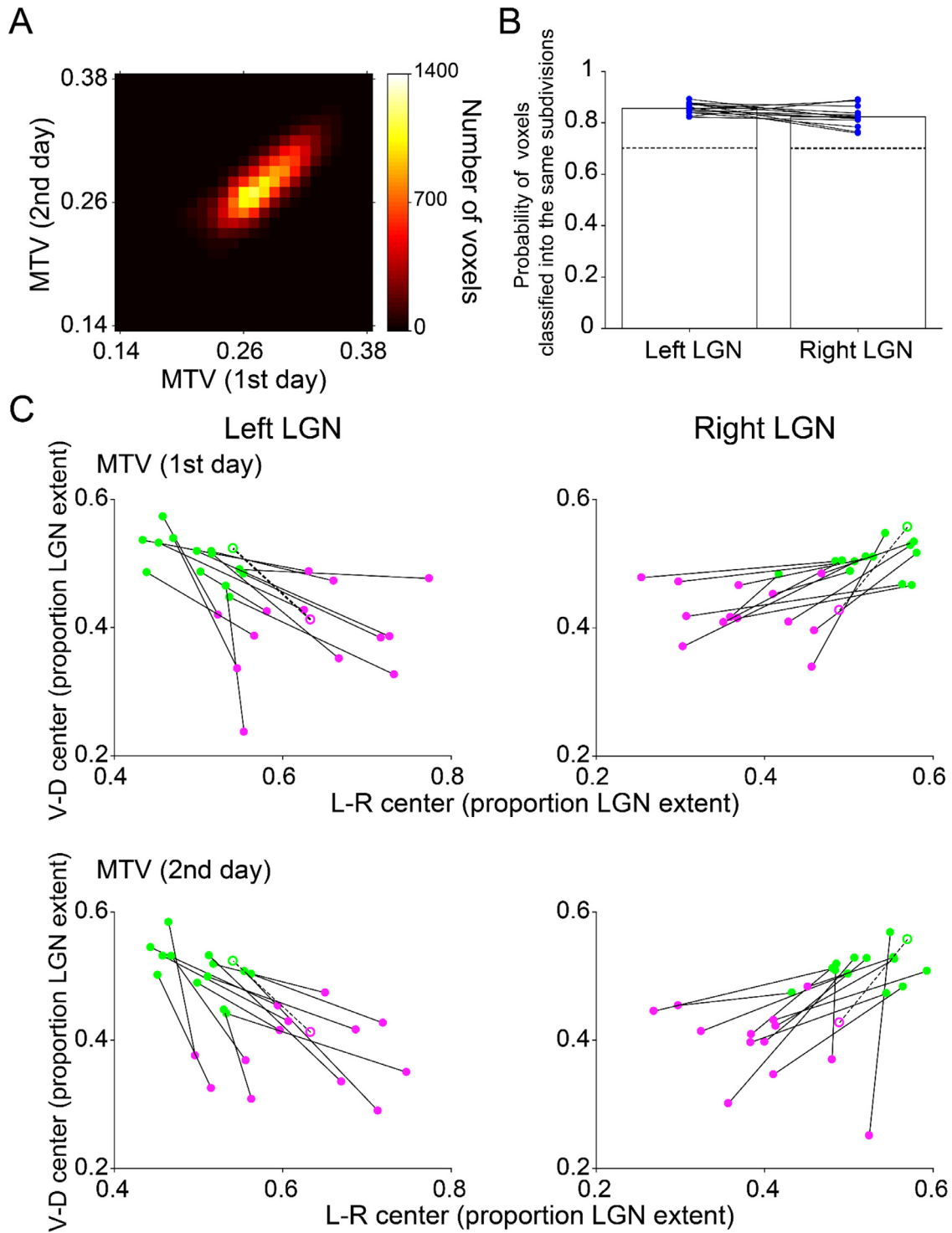


Fig. 7. Test–retest reproducibility of MTV-based parcellation. (A) Two-dimensional histogram comparing the MTV measurements across days in LGN voxels (horizontal axis, 1st day; vertical axis, 2nd day). The data are derived from LGN voxels pooled across subjects, who participated in the retest scans ($n = 13$; see Supplementary Fig. 12 for plots of individual subjects). The color map indicates the number of voxels. The intraclass correlation coefficient (ICC) of MTV measurements across days was 0.77. This high correlation coefficient indicated that the MTV measurements were reproducible across days. (B) Reproducibility of classification. The vertical axis depicts the probability that individual voxels were classified into the same LGN subdivisions between the test and retest dataset. The individual dots depict the results in individual hemispheres. The dotted lines depict the maximum probability of voxels being classified into the same subdivisions when randomly replacing the labels of subdivisions (M and P) among all voxels for 10,000 times. (C) The centers of the coordinates for the M and P subdivisions identified with MTV-based parcellation using the test (1st day) and retest (2nd day) datasets of subjects (filled circles and solid lines) who participated in the retest MTV measurement ($n = 13$). We replicated the results on the centers of M and P subdivisions in a consistent manner with those in BigBrain data (Amunts et al., 2013; open circles and dotted line). The plot of the test dataset was identical to Fig. 3 except for the number of subjects. The conventions are identical to those used in Fig. 3.

what types of microstructural differences lead to MTV differences between M and P subdivisions. In principle, the MTV quantifies non-water macromolecular volumes on the basis of calibrated quantitative PD maps (Mezer et al., 2013). Phantom experiments confirmed that MTV measurements correlate with the lipid fraction (Mezer et al., 2013; Filo et al., 2019; Shtangel and Mezer, 2020). However, there is no established theory on how much MTV variance in a particular brain area can be explained by specific types of microstructural properties. A number of histological studies on non-human primates reported differences in anatomical properties between M and P subdivisions, such as the higher neuronal cell density (Hassler, 1966; Yücel et al., 2000, 2003) and greater myelin content in the P subdivision (Pistorio et al., 2006). A recent post-mortem human study confirmed these properties (Müller-Axt et al., 2021). These results are in line with our results showing a larger MTV fraction in the P subdivision than in the M subdivision, since both a larger number of cells and greater myelin content will result in a larger lipid volume fraction. It is also possible that other neurobiological factors, such as glial cell density, partly explain the difference in MTV between the M and P subdivisions. This remains an open question for future investigations that compare quantitative MRI data with several different types of histological data registered in the same coordinate space (Alkemade et al., 2022) or that generate synthetic quantitative MRI data from histology data (Schurr and Mezer, 2021).

4.2. Advantage of MTV-based parcellation over other structural MRI methods

In standard practice, many neuroimaging studies have utilized T1w and/or T2w images to locate cortical areas or subcortical nuclei. While the relative values in these images are useful for identifying the borders between gray and white matter, their absolute values cannot be interpreted as being quantitative, because the measurements are affected by multiple sources of inhomogeneity such as B_1^+ inhomogeneity or coil gain bias. Recent developments in quantitative MRI have enabled the quantification of MRI parameters, which allows the comparison of brain tissue properties between human subjects (Mezer et al., 2013; Weiskopf et al., 2015; Forstmann et al., 2016; Keuken et al., 2017; Cercignani et al., 2018). These quantitative MRI measurements have provided valuable insights into the tissue properties of cortical areas (Sereno et al., 2013; Lutti et al., 2014; Carey et al., 2018) and white matter (Stüber et al., 2014; Schurr et al., 2018; Takemura et al., 2019).

Mezer et al. (2013) proposed MTV methods and demonstrated consistency of MTV measurements with lipid volume fractions in a phantom, high test–retest reproducibility, and sensitivity for white matter tissue changes in patients with multiple sclerosis. A strong advantage of this method is its independence from the static magnetic field strength, since it is based on PD measurements calibrated by assuming that the water fraction in CSF voxels is 100%. In fact, Mezer et al. (2013) demonstrated that MTV measurements in the brain are consistent across measurements performed using different types of hardware. Therefore, we chose MTV mapping as a potential method for parcellating the human LGN because it is relatively independent of hardware choices and thus useful for future clinical studies.

We found that MTV enabled the parcellation of the LGN in a consistent manner to that seen using histological data (Fig. 3), and subdivisions identified by MTV exhibited stimulus selectivity that was consistent with previous physiological studies (Fig. 4). MTV-based parcellation was superior to parcellation based on non-quantitative structural MRI maps (PD-weighted images or T1w/T2w maps; Fig. 6). This is most likely because the MTV was corrected for B_1^+ inhomogeneity, while the other maps were not. While the T1w/T2w map has been demonstrated to enhance tissue contrast and thus be useful for delineating borders between brain areas (Glasser and Van Essen, 2011) and has advantages in terms of shorter acquisition time, several studies demonstrated inconsistencies between T1w/T2w and quantitative MRI measurements that

were more sensitive to myelin (Arshad et al., 2017; Hagiwara et al., 2018; Uddin et al., 2018). These inconsistencies are most likely due to the fact that T1w/T2w images are not calibrated for B_1^+ inhomogeneity (Glasser and Van Essen, 2011). While we have not excluded the possibility that ad-hoc B_1^+ bias field correction (Glasser et al., 2013) may improve LGN parcellation using T1w/T2w images, our results demonstrated that MTV-based LGN parcellation performed better than T1w/T2w-based LGN parcellation, at least in the left hemisphere, most likely because of the superior calibrations for B_1^+ inhomogeneity in the LGN.

4.3. Comparison with fMRI-based LGN parcellation

A few fMRI studies have examined the spatial pattern of visually evoked BOLD signals in the LGN (Denison et al., 2014; Zhang et al., 2015). These studies demonstrated that clusters of LGN voxels preferentially respond to distinct types of visual stimuli, which was consistent with neurophysiological findings, suggesting that an approximate identification of the LGN subdivisions in living humans can be achieved using fMRI-based measurements of visual stimulus sensitivities. Quantitative structural MRI-based parcellation methods as shown in this study have several advantages compared with fMRI-based parcellation methods. First, the fMRI-based methods require a precise control of visual stimuli, which involves the presentation of isoluminant stimuli to selectively activate P subdivisions (Denison et al., 2014); this is unnecessary when using the structural MRI-based methods. Furthermore, the use of visual stimuli limits the application of LGN parcellation methods in clinical studies of patients with visual field loss or when using MRI scanners without visual stimulus presentation equipment. Second, structural MRI-based methods are more spatially precise, since the voxel size for MTV measurements (e.g., 1 mm isotropic voxels in this study) is generally smaller than those used in fMRI experiments (e.g., $1.8 \times 1.8 \times 1.5$ mm for 3T or 1.2–1.5 mm isotropic voxels for 7T in Denison et al., 2014). When using fMRI, large veins passing through multiple voxels can limit the spatial specificity of the BOLD signal (Uludağ and Blinder, 2018; Kay et al., 2019). Therefore, our methods are advantageous in terms of spatial precision. Finally, MTV-based parcellation has higher test–retest reliability across days (Fig. 7) compared with that reported previously in an fMRI study ($r < 0.4$; Denison et al., 2014). Therefore, MTV-based parcellation provides more stable identification of M and P subdivisions in individual living human brains. We note that fMRI-based identification of LGN subdivisions may be advantageous for coregistration to other functional maps compared with structural MRI-based methods because the image distortions are more similar between functional images than between structural and functional images. As fMRI-based methods are sure to improve (Huber et al., 2018; Kay et al., 2020), it is expected that the accuracy for dissociating BOLD activity between the M and P subdivisions will increase.

On a separate note, one could argue that the positive $\text{Beta}_{\text{Mstim-Pstim}}$ in the P subdivision observed in the fMRI experiment (Fig. 4) is counter-intuitive as neurons in the P subdivision should be more responsive to P-type stimuli. However, this result is consistent with a previous fMRI study using the same stimuli (Denison et al., 2014). We speculate that larger responses to M-type stimuli in P subdivisions may occur since 100% black–white luminance contrast stimuli (M-type stimuli) elicit very strong BOLD responses in general (Boynton et al., 1996). This idea is consistent with the findings of an electrophysiological study on the macaque LGN, which showed that, although P neurons have a lower contrast sensitivity than M neurons, the responses of P neurons increase as the luminance contrast increases (Derrington and Lennie, 1984). Although we might have obtained a more balanced response profile between the M-type and P-type stimuli if we lowered the luminance contrast of the M-type stimuli, such stimulus manipulation may limit the signal-to-noise ratio of BOLD responses evoked by the M-type stimuli. The optimization of visual stimulation protocols for LGN fMRI is thus an open question that should be resolved in future fMRI studies.

4.4. Related study

A recent study evaluated histological and quantitative T1 (qT1) MRI measurement on *ex vivo* human LGN sections (Müller-Axt et al., 2021). Their histological examination showed that cell and myelin densities are higher in P subdivisions than M subdivisions. They then demonstrated that high-resolution *ex vivo* qT1 measurements within the LGN can be used to classify M and P subdivisions. In addition, they acquired structural MRI data from living human brains using the MP2RAGE sequence and demonstrated that they can identify M and P subdivisions using the LGN population atlas averaged across subjects in a common reference space. This result is consistent with our study showing LGN-based parcellation based on *in vivo* MTV measurements using 3T MRI.

There are several differences between our work and Müller-Axt et al. (2021). First, Müller-Axt et al. (2021) and this study performed different types of validation. While Müller-Axt et al. (2021) compared high-resolution *ex vivo* qT1 mapping with multiple histological measurements, we compared MTV-based parcellation with BigBrain and fMRI-based stimulus selectivity measurements. These different types of comparisons performed in Müller-Axt et al. (2021) and our study provide comprehensive anatomical and physiological evidence on the validity to use quantitative structural MRI measurements to identify human LGN subdivisions. Second, we used 3T MRI while Müller-Axt et al. (2021) used 7T MRI. The value of this study is to demonstrate feasibility of structural MRI-based LGN parcellation in 3T, which is a more broadly accessible system for many investigators and closer to the clinical system. Taken together, Müller-Axt et al. (2021) and the present study provide complementary evidence on the utility of quantitative structural MRI method to estimate LGN subdivisions in living human brains.

4.5. Limitations and future directions

In this study, we classified voxels into M and P subdivisions using fixed volumetric ratios or a fixed threshold value based on MTV data pooled across subjects (Supplementary Fig. S10). Given that the volumetric ratio has some individual differences (Andrews et al., 1997) and can be different in some populations (e.g., patients with eye diseases), this procedure limits the applicability of MTV-based LGN parcellation to clinical populations. For this reason, it would be more ideal to classify the LGN voxels into M and P subdivisions by fitting a mixture model composed of two curves with distinct peaks to the distribution of the MTV fractions in each individual LGN without using any anatomical assumptions. However, this approach was not practical in this study because the MTV-based distribution of the LGN voxels in our *in vivo* data did not show two distinct peaks or skewed distributions corresponding to the M and P subdivisions (Supplementary Fig. S13). High-resolution *ex vivo* macaque magnetization transfer ratio (MTR) data (see Supplementary Materials and Supplementary Fig. S14) shows a skewed distribution of MTR values, with a longer tail for a lower MTR (which corresponds to M subdivision). This skewed distribution may be more consistent with that observed in a previous high-resolution *ex vivo* MRI study on the human brain (Müller-Axt et al., 2021). Therefore, if we could achieve MTV data acquisition with much higher spatial resolution in future work, one could expect a more skewed distribution and possibly two peaks of MTV in the LGN. For such a high-resolution dataset, the use of curve fitting to identify the M and P subdivisions may be practical as demonstrated in Müller-Axt et al. (2021).

The limited spatial resolution of the *in vivo* MTV data acquisition may have impacted the results and needs consideration. First, we could not fully exclude the partial volume effect of neighboring tissues and CSF as a potential confounder. However, the partial volume effect alone did not fully explain the results (Supplementary Fig. S11). Second, in some subjects, the MTV-based parcellation failed to identify the anterior part of the M subdivision, which was visible in BigBrain (Supplementary Figs.

S1–S3). This is likely because the anterior part of the M subdivision is small (Supplementary Fig. S15) and thus difficult to identify at the current spatial resolution. Therefore, improving spatial resolution will be essential for reducing a partial voluming effect and improving the accuracy of identifying the M subdivisions. In addition, thin koniocellular layers (K layers) are known to exist between each layer of the M and P subdivisions in the LGN (Guillery and Colonnier, 1970). Previous histological studies have indicated that the K layers have distinct anatomical properties compared with those in the M and P subdivisions (Hendry and Reid, 2000). Considering the location of K layers, the MTV fractions in many LGN voxels are likely to be affected by partial volumes between the K layers and M or P subdivisions. Therefore, part of the variance in the structural measurements may be affected by the anatomical properties of the K layers.

The MTV-based parcellation method proposed in this work has a relatively long acquisition time (60–90 min and 28 min for the PD-weighted image and quantitative structural MRI, respectively). This raises challenges in the application of this method to clinical routines. However, because the acquisition of all MRI data seems unnecessary to obtain reasonable MTV-based parcellation (see Supplementary Figs. S16 and S17 for the results when reducing the number of data used for analyses of MTV and PD-weighted image, respectively), performing studies on patients or larger numbers of healthy subjects using this method is not fully impractical.

This study focused on validating single-subject analyses of MTV-based parcellation of LGN subdivisions. To this end, we acquired data from 15 young adult subjects, to achieve acquisition of multiple types of data (fMRI and retest data) in the same individuals and to minimize individual variabilities derived from aging. On the other hand, since a previous study showed age dependency of the LGN volume (Li et al., 2012), it is important to extend this work by acquiring MTV data from a relatively large sample of aging populations to reveal how aging may impact the microstructural properties of the LGN subdivisions.

The MTV method itself may have room for improvement. For example, while the MTV method aims to minimize the T2* effect by using a short TE (Mezer et al., 2013, 2016), it is possible that some T2* effect may still be present in the MTV maps. In the future, it is important to investigate the extent to which the removal of T2* contributions from MTV maps may affect MTV-based LGN parcellation by acquiring data using multiple TEs (Abbas et al., 2015).

Despite the aforementioned limitations, an extension of MTV-based LGN parcellation methods proposed in this work may open opportunities for future clinical and neuroscience studies since it enables measurement of the LGN in living humans and thus can be analyzed together with other clinical, behavioral and functional measurements. Potential applications may include comparisons between tissue properties of the M subdivisions and deficits of visual motion discrimination performance observed in clinical populations such as glaucoma and dyslexia (Chase and Jenner, 1993; Felmingham and Jakobson, 1995; Demb et al., 1998; Stein, 2001; Main et al., 2014; Maddess et al., 1992; Cello et al., 2000) by acquiring MTV data with psychophysical or clinical data from the same individual subjects. Alternatively, one can also investigate the covariance of MTV between LGN subdivisions and other parts of the visual system to learn how different parts of the visual system mature together during the development of living humans (Andrews et al., 1997; Miyata et al., 2022). However, at this point, there is a caveat in using a proposed MTV-based parcellation method relying on fixed volume ratio between M and P subdivisions to clinical populations, since such ratio itself may be affected by disorders. Therefore, addressing these future research questions may require further improvements on methods, which enables data acquisition with higher spatial resolution and data analysis without prior assumptions of volumetric ratio between subdivisions. We hope that extensions of this study will provide more concrete methods to investigate how the properties of LGN subdivisions are related to the organization, functions, and disorders of the human visual system.

5. Conclusion

We propose a method to identify M and P subdivisions of LGN in individual living humans by combining two structural MR measures: high-resolution PD-weighted images and MTV maps. MTV measurements within the LGN showed a consistent pattern with the previously known anatomical differences between the M and P subdivisions in *ex vivo* human and non-human primate brains. Moreover, we demonstrated the validity of the method to identify M and P subdivisions based on MTV in each individual brain, by showing that: (1) the locations of the defined M and P subdivisions were consistent with that from a postmortem human brain, (2) the defined M and P subdivisions showed significantly different stimulus selectivities in a consistent manner with the known functional difference between these subdivisions, and (3) the M and P subdivisions were robustly identified using remeasured MTV data. This method will open an avenue for direct comparisons of LGN subdivision properties with behavioral or functional data or evaluating the consequence of visual disorders on LGN tissue properties using a widely accessible 3T MRI system.

Declaration of Competing Interest

The authors declare no competing interests.

Credit authorship contribution statement

Hiroki Oishi: Conceptualization, Methodology, Software, Validation, Formal analysis, Investigation, Data curation, Writing – original draft, Writing – review & editing, Visualization, Funding acquisition. **Hiomasa Takemura:** Conceptualization, Methodology, Writing – original draft, Writing – review & editing, Supervision, Project administration, Funding acquisition. **Kaoru Amano:** Conceptualization, Writing – original draft, Writing – review & editing, Supervision, Project administration, Funding acquisition.

Data availability

We have shared the data at the online repository (<https://osf.io/7gcx5>).

Acknowledgments

We thank Yusuke Sakai for supporting data curation and analysis and Taiki Aoyama for supporting data analysis. We also thank Frank Q. Ye and David A. Leopold for providing the *ex vivo* macaque MTR dataset. This work was supported by the Japan Society for the Promotion of Science (JSPS) KAKENHI (JP20J11101 to HO, JP17H04684 and JP21H03789 to HT). The funders had no role in the study design, data collection and interpretation, or the decision to submit the work for publication.

Supplementary materials

Supplementary material associated with this article can be found, in the online version, at doi:[10.1016/j.neuroimage.2022.119777](https://doi.org/10.1016/j.neuroimage.2022.119777).

References

Abbas, Z., Gras, V., Möllenhoff, K., Oros-Peusquens, A.M., Shah, N.J., 2015. Quantitative water content mapping at clinically relevant field strengths: a comparative study at 1.5 T and 3 T. *Neuroimage* 106, 404–413.

Alkemade, A., Bazin, P.L., Balesar, R., Pine, K., Kirilina, E., Möller, H.E., Trampel, R., Kros, J.M., Keuken, M.C., Bleys, R.L.A.W., Swaab, D.F., Herrler, A., Weiskopf, N., Forstmann, B.U., 2022. A unified 3D map of microscopic architecture and MRI of the human brain. *Sci. Adv.* 8, eabj7892.

Amunts, K., Lepage, C., Borgeat, L., Mohlberg, H., Dickscheid, T., Rousseau, M.É., Bludau, S., Bazin, P.L., Lewis, L.B., Oros-Peusquens, A.M., Shah, N.J., Lippert, T., Zilles, K., Evans, A.C., 2013. BigBrain: an ultrahigh-resolution 3D human brain model. *Science* 340, 1472–1475.

Andrews, T.J., Halpern, S.D., Purves, D., 1997. Correlated size variations in human visual cortex, lateral geniculate nucleus, and optic tract. *J. Neurosci.* 17, 2859–2868.

Atapour, N., Worthy, K.H., Rosa, M.G.P., 2021. Neurochemical changes in the primate lateral geniculate nucleus following lesions of striate cortex in infancy and adulthood: implications for residual vision and blindsight. *Brain Struct. Funct.* 226, 2763–2775.

Arshad, M., Stanley, J.A., Raz, N., 2017. Test-retest reliability and concurrent validity of *in vivo* myelin content indices: myelin water fraction and calibrated T1 w/T2 w image ratio. *Hum. Brain Mapp.* 38, 1780–1790.

Bakken, T.E., van Velthoven, C.T.J., Menon, V., Hodge, R.D., Yao, Z., Nguyen, T.N., Graybuck, L.T., Horwitz, G.D., Bertagnolli, D., Goldy, J., Yanny, A.M., Garren, E., Parry, S., Casper, T., Shehata, S.I., Barkan, E.R., Szafer, A., Levi, B.P., Dee, N., Smith, K.A., Sunkin, S.M., Bernard, A., Phillips, J., Hawrylycz, M.J., Koch, C., Murphy, G.J., Lein, E., Zeng, H., Tasic, B., 2021. Single-cell and single-nucleus RNA-seq uncovers shared and distinct axes of variation in dorsal LGN neurons in mice, non-human primates, and humans. *Elife* 10, e64875.

Ban, H., Yamamoto, H., 2013. A non-device-specific approach to display characterization based on linear, nonlinear, and hybrid search algorithms. *J. Vis.* 13 (6), 20.

Barral, J.K., Gudmundson, E., Stikov, N., Etezadi-Amoli, M., Stoica, P., Nishimura, D.G., 2010. A robust methodology for *in vivo* T1 mapping. *Magn. Reson. Med.* 64, 1057–1067.

Benson, N.C., Winawer, J., 2018. Bayesian analysis of retinotopic maps. *Elife* 7, e40224.

Berman, S., West, K.L., Does, M.D., Yeatman, J.D., Mezer, A.A., 2018. Evaluating g-ratio weighted changes in the corpus callosum as a function of age and sex. *Neuroimage* 182, 304–313.

Boynton, G.M., Engel, S.A., Glover, G.H., Heeger, D.J., 1996. Linear systems analysis of functional magnetic resonance imaging in human V1. *J. Neurosci.* 16, 4207–4221.

Bridge, H., Bell, A.H., Ainsworth, M., Sallet, J., Premereur, E., Ahmed, B., Mitchell, A.S., Schüffelgen, U., Buckley, M., Tendler, B.C., Miller, K.L., Mars, R.B., Parker, A.J., Krug, K., 2019. Preserved extrastriate visual network in a monkey with substantial, naturally occurring damage to primary visual cortex. *Elife* 8, e42325.

Carey, D., Caprini, F., Allen, M., Lutti, A., Weiskopf, N., Rees, G., Callaghan, M.F., Dick, F., 2018. Quantitative MRI provides markers of intra-, inter-regional, and age-related differences in young adult cortical microstructure. *Neuroimage* 182, 429–440.

Cello, K.E., Nelson-Quigg, J.M., Johnson, C.A., 2000. Frequency doubling technology perimetry for detection of glaucomatous visual field loss. *Am. J. Ophthalmol.* 129, 314–322.

Cercignani, M., Dowell, N.G., Tofts, P.S., 2018. *Quantitative MRI of the Brain: Principles of Physical Measurement*, 2nd ed. CRC Press.

Chase, C., Jenner, A.R., 1993. Magnocellular visual deficits affect temporal processing of dyslexics. *Ann. N. Y. Acad. Sci.* 682, 326–329.

Csernansky, J.G., Schindler, M.K., Splinter, N.R., Wang, L., Gado, M., Selemon, L.D., Rastogi-Cruz, D., Posener, J.A., Thompson, P.A., Miller, M.I., 2004. Abnormalities of thalamic volume and shape in schizophrenia. *Am. J. Psychiatry* 161, 896–902.

Demb, J.B., Boynton, G.M., Best, M., Heeger, D.J., 1998. Psychophysical evidence for a magnocellular pathway deficit in dyslexia. *Vis. Res.* 38, 1555–1559.

Denison, R.N., Vu, A.T., Yacoub, E., Feinberg, D.A., Silver, M.A., 2014. Functional mapping of the magnocellular and parvocellular subdivisions of human LGN. *Neuroimage* 102 (Pt 2), 358–369.

Derrington, A.M., Lennie, P., 1984. Spatial and temporal contrast sensitivities of neurons in lateral geniculate nucleus of macaque. *J. Physiol.* 357, 219–240.

DeYoe, E.A., Bandettini, P., Neitz, J., Miller, D., Winans, P., 1994. Functional magnetic resonance imaging (fMRI) of the human brain. *J. Neurosci. Methods* 54, 171–187.

Dumoulin, S.O., Wandell, B.A., 2008. Population receptive field estimates in human visual cortex. *Neuroimage* 39, 647–660.

Duval, T., Le Vy, S., Stikov, N., Campbell, J., Mezer, A., Witzel, T., Keil, B., Smith, V., Wald, L.L., Klawiter, E., Cohen-Adad, J., 2017. g-Ratio weighted imaging of the human spinal cord *in vivo*. *Neuroimage* 145, 11–23.

Engel, S.A., Rumelhart, D.E., Wandell, B.A., Lee, A.T., Glover, G.H., Chichilnisky, E.J., Shadlen, M.N., 1994. fMRI of human visual cortex. *Nature* 369, 525.

Felmingham, K.L., Jakobson, L.S., 1995. Visual and visuomotor performance in dyslexic children. *Exp. Brain Res.* 106, 467–474.

Filo, S., Shtangel, O., Salamon, N., Kol, A., Weisinger, B., Shifman, S., Mezer, A.A., 2019. Disentangling molecular alterations from water-content changes in the aging human brain using quantitative MRI. *Nat. Commun.* 10, 3403.

Fonov, V., Evans, A.C., Botteron, K., Almli, C.R., McKinstry, R.C., Collins, D.L. Brain Development Cooperative Group, 2011. Unbiased average age-appropriate atlases for pediatric studies. *Neuroimage* 54, 313–327.

Fonov, V.S., Evans, A.C., McKinstry, R.C., Almli, C.R., Collins, D.L., 2009. Unbiased non-linear average age-appropriate brain templates from birth to adulthood. *Neuroimage* 47 (Supplement 1), S102.

Forstmann, B.U., de Hollander, G., van Maanen, L., Alkemade, A., Keuken, M.C., 2016. Towards a mechanistic understanding of the human subcortex. *Nat. Rev. Neurosci.* 18, 57.

Giraldo-Chica, M., Schneider, K.A., 2018. Hemispheric asymmetries in the orientation and location of the lateral geniculate nucleus in dyslexia. *Dyslexia* 24, 197–203.

Glasser, M.F., Coalson, T.S., Robinson, E.C., Hacker, C.D., Harwell, J., Yacoub, E., Ugurbil, K., Andersson, J., Beckmann, C.F., Jenkinson, M., Smith, S.M., Van Essen, D.C., 2016. A multi-modal parcellation of human cerebral cortex. *Nature* 536, 171–178.

Glasser, M.F., Sotiropoulos, S.N., Wilson, J.A., Coalson, T.S., Fischl, B., Andersson, J.L., Xu, J., Jbabdi, S., Webster, M., Polimeni, J.R., Van Essen, D.C., Jenkinson, M., Consortium, W., U-Minn, H.C.P., 2013. The minimal preprocessing pipelines for the human connectome project. *Neuroimage* 80, 105–124.

Glasser, M.F., Van Essen, D.C., 2011. Mapping human cortical areas *in vivo* based on myelin content as revealed by T1- and T2-weighted MRI. *J. Neurosci.* 31, 11597–11616.

Güllery, R.W., Colonnier, M., 1970. Synaptic patterns in the dorsal lateral geniculate nucleus of the monkey. *Z. Zellforsch. Mikrosk. Anat.* 103, 90–108.

- Gupta, N., Ang, L.C., Noël de Tilly, L., Bidaisee, L., Yücel, Y.H., 2006. Human glaucoma and neural degeneration in intracranial optic nerve, lateral geniculate nucleus, and visual cortex. *Br. J. Ophthalmol.* 90, 674–678.
- Hagiwara, A., Hori, M., Kamagata, K., Warntjes, M., Matsuyoshi, D., Nakazawa, M., Ueda, R., Andica, C., Koshino, S., Maekawa, T., Irie, R., Takamura, T., Kumamaru, K.K., Abe, O., Aoki, S., 2018. Myelin measurement: comparison between simultaneous tissue relaxometry, magnetization transfer saturation index, and T_1w/T_2w ratio methods. *Sci. Rep.* 8, 10554.
- Hassler, R., 1966. Comparative anatomy of the central visual systems in day- and night-active primates. In: *Evolution of the Forebrain*. Springer, Boston, MA, pp. 419–434.
- Haynes, J.D., Deichmann, R., Rees, G., 2005. Eye-specific effects of binocular rivalry in the human lateral geniculate nucleus. *Nature* 438, 496–499.
- Hendry, S.H.C., Reid, R.C., 2000. The koniocellular pathway in primate vision. *Annu. Rev. Neurosci.* 23, 127–153.
- Hickey, T.L., Guillery, R.W., 1979. Variability of laminar patterns in the human lateral geniculate nucleus. *J. Comp. Neurol.* 183, 221–246.
- Huber, L., Ivanov, D., Handwerker, D.A., Marrett, S., Guidi, M., Uludağ, K., Bandettini, P.A., Poser, B.A., 2018. Techniques for blood volume fMRI with VASO: from low-resolution mapping towards sub-millimeter layer-dependent applications. *Neuroimage* 164, 131–143.
- Hughes, S.W., Lőrincz, M., Cope, D.W., Blethyn, K.L., Kékesi, K.A., Parri, H.R., Juhász, G., Crunelli, V., 2004. Synchronized oscillations at alpha and theta frequencies in the lateral geniculate nucleus. *Neuron* 42, 253–268.
- Ives, H.E., 1912. XII. Studies in the photometry of lights of different colours. *Lond. Edinb. Dublin Philos. Mag. J. Sci.* 24, 149–188.
- Jenkinson, M., Bannister, P., Brady, M., Smith, S., 2002. Improved optimization for the robust and accurate linear registration and motion correction of brain images. *Neuroimage* 17, 825–841.
- Joffe, K.M., Raymond, J.E., Chricton, A., 1997. Motion coherence perimetry in glaucoma and suspected glaucoma. *Vis. Res.* 37, 955–964.
- Kay, K., Jamison, K.W., Vizoli, L., Zhang, R., Margalit, E., Uğurbil, K., 2019. A critical assessment of data quality and venous effects in sub-millimeter fMRI. *Neuroimage* 189, 847–869.
- Kay, K., Jamison, K.W., Zhang, R.Y., Uğurbil, K., 2020. A temporal decomposition method for identifying venous effects in task-based fMRI. *Nat. Methods* 17, 1033–1039.
- Keuken, M.C., Bazin, P.L., Backhouse, K., Beekhuizen, S., Himmer, L., Kandola, A., Lafeber, J.J., Prochazkova, L., Trutti, A., Schäfer, A., Turner, R., Forstmann, B.U., 2017. Effects of aging on T_1 , T_2^* , and QSM MRI values in the subcortex. *Brain Struct. Funct.* 222, 2487–2505.
- Li, M., He, H.G., Shi, W., Li, J., Lv, B., Wang, C.H., Miao, Q.W., Wang, Z.C., Wang, N.L., Walter, M., Sabel, B.A., 2012. Quantification of the human lateral geniculate nucleus *in vivo* using MR imaging based on morphometry: volume loss with age. *AJNR Am. J. Neuroradiol.* 33, 915–921.
- Ling, S., Pratte, M.S., Tong, F., 2015. Attention alters orientation processing in the human lateral geniculate nucleus. *Nat. Neurosci.* 18, 496–498.
- Liu, Z., de Zwart, J.A., Yao, B., van Gelderen, P., Kuo, L.W., Duyn, J.H., 2012. Finding thalamic BOLD correlates to posterior alpha EEG. *Neuroimage* 63, 1060–1069.
- Livingstone, M., Hubel, D., 1988. Segregation of form, color, movement, and depth: anatomy, physiology, and perception. *Science* 240, 740–749.
- Lutti, A., Dick, F., Sereno, M.I., Weiskopf, N., 2014. Using high-resolution quantitative mapping of R1 as an index of cortical myelination. *Neuroimage* 93 (Pt 2), 176–188.
- Maddess, T.L., Henry, G.H., Others, 1992. Performance of nonlinear visual units in ocular hypertension and glaucoma. *Clin. Vis. Sci.* 7, 371–383.
- Main, K.L., Pestilli, F., Mezer, A., Yeatman, J., Martin, R., Phipps, S., Wandell, B., 2014. Speed discrimination predicts word but not pseudo-word reading rate in adults and children. *Brain Lang.* 138, 27–37.
- Mcketton, L., Kelly, K.R., Schneider, K.A., 2014. Abnormal lateral geniculate nucleus and optic chiasm in human albinism. *J. Comp. Neurol.* 522, 2680–2687.
- Mezer, A., Rokem, A., Berman, S., Hastie, T., Wandell, B.A., 2016. Evaluating quantitative proton-density-mapping methods. *Hum. Brain Mapp.* 37, 3623–3635.
- Mezer, A., Yeatman, J.D., Stikov, N., Kay, K.N., Cho, N.J., Dougherty, R.F., Perry, M.L., Parvizi, J., Hua le, H., Butts-Pauly, K., Wandell, B.A., 2013. Quantifying the local tissue volume and composition in individual brains with magnetic resonance imaging. *Nat. Med.* 19, 1667–1672.
- Minami, S., Amano, K., 2017. Illusory jitter perceived at the frequency of alpha oscillations. *Curr. Biol.* 27, 2344–2351 e4.
- Minami, S., Oishi, H., Takemura, H., Amano, K., 2020. Inter-individual differences in occipital alpha oscillations correlate with white matter tissue properties of the optic radiation. *eNeuro* 7, 1–11 ENEURO.0224-19.2020.
- Miyata, T., Benson, N.C., Winawer, J., Takemura, H., 2022. Structural covariance and heritability of the optic tract and primary visual cortex in living human brains. *J. Neurosci.* 42, 6761–6769.
- Moeller, S., Yacoub, E., Olman, C.A., Auerbach, E., Strupp, J., Harel, N., Uğurbil, K., 2010. Multiband multislice GE-EPI at 7 tesla, with 16-fold acceleration using partial parallel imaging with application to high spatial and temporal whole-brain fMRI. *Magn. Reson. Med.* 63, 1144–1153.
- Müller-Axt, C., Eichner, C., Rusch, H., Kauffmann, L., Bazin, P.L., Anwender, A., Morawski, M., von Kriegstein, K., 2021. Mapping the human lateral geniculate nucleus and its cytoarchitectonic subdivisions using quantitative MRI. *Neuroimage* 244, 118559.
- Nassi, J.J., Callaway, E.M., 2009. Parallel processing strategies of the primate visual system. *Nat. Rev. Neurosci.* 10, 360–372.
- O'Connor, D.H., Fukui, M.M., Pinsk, M.A., Kastner, S., 2002. Attention modulates responses in the human lateral geniculate nucleus. *Nat. Neurosci.* 5, 1203–1209.
- Oishi, H., Takemura, H., Aoki, S.C., Fujita, I., Amano, K., 2018. Microstructural properties of the vertical occipital fasciculus explain the variability in human stereoacuity. *Proc. Natl. Acad. Sci. U. S. A.* 115, 12289–12294.
- Patenaude, B., Smith, S.M., Kennedy, D.N., Jenkinson, M., 2011. A Bayesian model of shape and appearance for subcortical brain segmentation. *Neuroimage* 56, 907–922.
- Pistorio, A.L., Hendry, S.H., Wang, X., 2006. A modified technique for high-resolution staining of myelin. *J. Neurosci. Methods* 153, 135–146.
- Schiller, P.H., Logothetis, N.K., Charles, E.R., 1990. Functions of the colour-opponent and broad-band channels of the visual system. *Nature* 343, 68–70.
- Schmid, M.C., Mrowka, S.W., Turchi, J., Saunders, R.C., Wilke, M., Peters, A.J., Ye, F.Q., Leopold, D.A., 2010. Blindsight depends on the lateral geniculate nucleus. *Nature* 466, 373–377.
- Schneider, K.A., Kastner, S., 2009. Effects of sustained spatial attention in the human lateral geniculate nucleus and superior colliculus. *J. Neurosci.* 29, 1784–1795.
- Selemon, L.D., Begovic, A., 2007. Stereologic analysis of the lateral geniculate nucleus of the thalamus in normal and schizophrenic subjects. *Psychiatry Res.* 151, 1–10.
- Sereno, M.I., Dale, A.M., Reppas, J.B., Kwong, K.K., Belliveau, J.W., Brady, T.J., Rosen, B.R., Tootell, R.B., 1995. Borders of multiple visual areas in humans revealed by functional magnetic resonance imaging. *Science* 268, 889–893.
- Sereno, M.I., Lutti, A., Weiskopf, N., Dick, F., 2013. Mapping the human cortical surface by combining quantitative T_1 with retinotopy. *Cereb. Cortex* 23, 2261–2268.
- Shams, Z., Norris, D.G., Marques, J.P., 2019. A comparison of *in vivo* MRI based cortical myelin mapping using T_1w/T_2w and R1 mapping at 3T. *PLoS One* 14, e0218089.
- Schurr, R., Duan, Y., Norcia, A.M., Ogawa, S., Yeatman, J.D., Mezer, A.A., 2018. Tractography optimization using quantitative T1 mapping in the human optic radiation. *Neuroimage* 181, 645–658.
- Schurr, R., Mezer, A.A., 2021. The glial framework reveals white matter fiber architecture in human and primate brains. *Science* 374, 762–767.
- Shtangel, O., Mezer, A.A., 2020. A phantom system for assessing the effects of membrane lipids on water proton relaxation. *NMR Biomed.* 33, e4209.
- Stein, J., 2001. The magnocellular theory of developmental dyslexia. *Dyslexia* 7, 12–36.
- Stüber, C., Morawski, M., Schafer, A., Labadie, C., Wahnert, M., Leuze, C., Streicher, M., Barapatre, N., Reimann, K., Geyer, S., Spemann, D., Turner, R., 2014. Myelin and iron concentration in the human brain: a quantitative study of MRI contrast. *Neuroimage* 93 (Pt 1), 95–106.
- Takemura, H., Ogawa, S., Mezer, A.A., Horiguchi, H., Miyazaki, A., Matsumoto, K., Shikishima, K., Nakano, T., Masuda, Y., 2019. Diffusivity and quantitative T1 profile of human visual white matter tracts after retinal ganglion cell damage. *Neuroimage Clin.* 23, 101826.
- Uddin, M.N., Figley, T.D., Marrie, R.A., Figley, C.R., COMS Study Group, 2018. Can T_1w/T_2w ratio be used as a myelin-specific measure in subcortical structures? Comparisons between FSE-based T_1w/T_2w ratios, GRASE-based T_1w/T_2w ratios and multi-echo GRASE-based myelin water fractions. *NMR Biomed.* 31. doi:10.1002/nbm.3868.
- Uludağ, K., Blinder, P., 2018. Linking brain vascular physiology to hemodynamic response in ultra-high field MRI. *Neuroimage* 168, 279–295.
- Usrey, W.M., Reid, R.C., 2000. Visual physiology of the lateral geniculate nucleus in two species of new world monkey: saimiri sciureus and Aotus trivirgatus. *J. Physiol.* 523 (Pt 3), 755–769.
- Viviano, J.D., Schneider, K.A., 2015. Interhemispheric interactions of the human thalamic reticular nucleus. *J. Neurosci.* 35, 2026–2032.
- Wandell, B.A., Winawer, J., 2011. Imaging retinotopic maps in the human brain. *Vis. Res.* 51, 718–737.
- Wandell, B.A., Winawer, J., 2015. Computational neuroimaging and population receptive fields. *Trends Cogn. Sci.* 19, 349–357.
- Weiskopf, N., Mohammadi, S., Lutti, A., Callaghan, M.F., 2015. Advances in MRI-based computational neuroanatomy: from morphometry to *in-vivo* histology. *Curr. Opin. Neurol.* 28, 313–322.
- Yeshurun, Y., Levy, L., 2003. Transient spatial attention degrades temporal resolution. *Psychol. Sci.* 14, 225–231.
- Yücel, Y.H., Zhang, Q., Gupta, N., Kaufman, P.L., Weinreb, R.N., 2000. Loss of neurons in magnocellular and parvocellular layers of the lateral geniculate nucleus in glaucoma. *Arch. Ophthalmol.* 118, 378–384.
- Yücel, Y.H., Zhang, Q., Weinreb, R.N., Kaufman, P.L., Gupta, N., 2003. Effects of retinal ganglion cell loss on magno-, parvo-, koniocellular pathways in the lateral geniculate nucleus and visual cortex in glaucoma. *Prog. Retin. Eye Res.* 22, 465–481.
- Yu, Q., Zhang, P., Qiu, J., Fang, F., 2016. Perceptual learning of contrast detection in the human lateral geniculate nucleus. *Curr. Biol.* 26, 3176–3182.
- Zhang, P., Wen, W., Sun, X., He, S., 2016. Selective reduction of fMRI responses to transient achromatic stimuli in the magnocellular layers of the LGN and the superficial layer of the SC of early glaucoma patients. *Hum. Brain Mapp.* 37, 558–569.
- Zhang, P., Zhou, H., Wen, W., He, S., 2015. Layer-specific response properties of the human lateral geniculate nucleus and superior colliculus. *Neuroimage* 111, 159–166.
- Zhang, Y., Brady, M., Smith, S., 2001. Segmentation of brain MR images through a hidden Markov random field model and the expectation-maximization algorithm. *IEEE Trans. Med. Imaging* 20, 45–57.